VORTEX FILAMENT EQUATION FOR A REGULAR POLYGON IN THE HYPERBOLIC PLANE

FRANCISCO DE LA HOZ, SANDEEP KUMAR, AND LUIS VEGA

Abstract. The aim of this article is twofold. First, we show the evolution of the vortex filament equation (VFE) for a regular planar polygon in the hyperbolic space. Unlike in the Euclidean space, the planar polygon is open and both of its ends grow exponentially, which makes the problem more challenging from a numerical point of view. However, with fixed boundary conditions, a finite difference scheme and a fourth-order Runge–Kutta method in time, we show that the numerical solution is in complete agreement with the one obtained from algebraic techniques. Second, as in the Euclidean case, we claim that, at infinitesimal times, the evolution of VFE for a planar polygon as the initial datum can be described as a superposition of several one-corner initial data. As a consequence, not only can we compute the speed of the center of mass of the planar polygon, but the relationship also allows us to compare the time evolution of any of its corners with that in the Euclidean case.

1. Introduction

Consider the binormal flow

$$\mathbf{X}_t = \kappa \mathbf{b}, \tag{1}$$

where t is the time, κ the curvature and $\mathbf{b}$ the binormal component of the Frenet–Serret formulas. As an approximation of the dynamics of a vortex filament (represented by $\mathbf{X}$) under Euler equations, (1) first appeared in the work of Da Rios in 1906, and was later rederived by Arms and Hama in 1965 [1, 2]. This model is commonly known as the vortex filament equation (VFE). The flow, also called the localized induction approximation (LIA), can be expressed as

$$\mathbf{X}_t = \mathbf{X}_s \wedge_+ \mathbf{X}_{ss}, \tag{2}$$

where s is the arc-length parameter, and $\wedge_+$ is the usual cross product. The tangent vector $\mathbf{T} = \mathbf{X}_s$ satisfies

$$\mathbf{T}_t = \mathbf{T} \wedge_+ \mathbf{T}_{ss}, \tag{3}$$

and, during the time evolution, it preserves its magnitude, so we can assume that it takes values in the unit sphere. Equation (3) is called the Schrödinger map equation onto the sphere and can be expressed in a more geometric way as

$$\mathbf{T}_t = \mathbf{J}\mathbf{D}_s\mathbf{T}_s, \tag{4}$$

where $\mathbf{D}_s$ is the covariant derivative and $\mathbf{J}$ is the complex structure of the sphere. By writing it in this way, (3) can be extended to more general definition domains and images [3]. For instance, when the target space is chosen as $\mathbb{H}^2 = \{(x_1, x_2, x_3) : -x_1^2 + x_2^2 + x_3^2 = -1, x_1 > 0\}$, i.e., a unit

Date: October 14, 2021.

sphere in Minkowski 3-space $\mathbb{R}^{1,2} = \{(x_1, x_2, x_3) : ds^2 = -dx_1^2 + dx_2^2 + dx_3^2\}$, the equivalent of (3) is [4]

$$\mathbf{T}_t = \mathbf{T} \wedge_- \mathbf{T}_{ss}, \tag{5}$$

and that of (2) is

$$\mathbf{X}_t = \mathbf{X}_s \wedge_- \mathbf{X}_{ss}, \tag{6}$$

where $\mathbf{X} \in \mathbb{R}^{1,2}$, $\mathbf{T} \in \mathbb{H}^2$, and the Minkowski cross product $\wedge_-$ is defined by [5]

$$\mathbf{a} \wedge_- \mathbf{b} = (-(a_2b_3 - a_3b_2), a_3b_1 - a_1b_3, a_1b_2 - a_2b_1), \ \mathbf{a}, \mathbf{b} \in \mathbb{R}^{1,2}.$$

Equivalently, the Minkowski pseudo-scalar product is given by

$$\mathbf{a} \circ_- \mathbf{b} = -a_1b_1 + a_2b_2 + a_3b_3,$$

which defines

$$|\mathbf{a}|_0^2 = \mathbf{a} \circ_- \mathbf{a}. \tag{7}$$

Thus, depending on whether $|\cdot|_0$ is positive, zero, or positive imaginary, the corresponding vector can be classified as *space-like*, *light-like*, or *time-like*, respectively. Since $\mathbf{T} \in \mathbb{H}^2$, the corresponding $\mathbf{X}$ is called a time-like curve [6, 5]. Note that depending on the sign of the first component of a time-like vector, it can be further classified as *positive* or *negative time-like*; for instance, in the definition of $\mathbb{H}^2$ given above, we have considered only the positive time-like vectors. Let us also define the *time-like angle* between two positive (respectively, negative) time-like vectors $\mathbf{a}$ and $\mathbf{b}$ as the unique nonnegative real number $\sigma(\mathbf{a}, \mathbf{b})$, such that

$$\mathbf{a} \circ_- \mathbf{b} = -|\mathbf{a}|_0|\mathbf{b}|_0 \cosh(\sigma(\mathbf{a}, \mathbf{b})).$$

Moreover, in this work, we deal with vectors that are positive time-like; for simplicity of notation, we refer to them as time-like. On the other hand, for a sufficiently smooth curve $\mathbf{X}$ with curvature κ and torsion τ, the equivalent of the Frenet–Serret formulas in the hyperbolic setting is given by

$$\begin{pmatrix} \mathbf{T} \\ \mathbf{n} \\ \mathbf{b} \end{pmatrix}_s = \begin{pmatrix} 0 & \kappa & 0 \\ \kappa & 0 & \tau \\ 0 & -\tau & 0 \end{pmatrix} . \begin{pmatrix} \mathbf{T} \\ \mathbf{n} \\ \mathbf{b} \end{pmatrix}, \tag{8}$$

where the normal vector $\mathbf{n}$ and binormal vector $\mathbf{b}$ are space-like and, along with $\mathbf{T}$, form an orthonormal system [6]. With this, the corresponding filament function,

$$\psi(s,t) = \kappa(s,t) e^{i \int_0^s \tau(s',t) ds'}, \tag{9}$$

transforms (5)-(6) into the defocusing nonlinear Schrödinger (NLS) equation [7]:

$$\psi_t = i\psi_{ss} - \frac{i}{2}\psi(|\psi|^2 + A(t)), \ A(t) \in \mathbb{R}. \tag{10}$$

Note that VFE is time reversible, i.e., if $\mathbf{X}(s,t)$ is a solution, then so is $\mathbf{X}(-s,-t)$. Bearing this in mind, an important property of VFE and hence, of the Schrödinger map, is that it has a one-parameter family of regular self-similar solutions that develop a corner-shaped singularity in finite time. In other words, at the time of the formation of the singularity, i.e., $t = 0$, the curve $\mathbf{X}$ has a corner, its tangent vector is a Heaviside-type function, and ψ is a Dirac delta located at $s = 0$. This was shown in [8] for the Euclidean case, and the hyperbolic case was studied in [9] (from now on, it will be referred to as the one-corner problem). Moreover, the well-posedness of the problem in the elliptic case has been established through a series of papers by Banica and Vega [10, 11, 12, 13].

On the other hand, the numerical study of the self-similar solutions was first done in [14], and later in [15], where both the Euclidean and hyperbolic cases were considered. In [15], not only the formation of the singularity was captured, but the authors also started with a corner-shaped initial datum and recovered the self-similar solutions numerically. In all the cases, the choice of boundary conditions was found to be crucial.

Although the problem of a curve with one corner otherwise smooth has been well-understood both theoretically and numerically, the case of a polygonal curve has gained attention only recently [16, 17]. In [18], a regular planar polygon with M sides (from now on, it will be referred to as the planar M-polygon) was considered as an initial curve in the Euclidean case, and using algebraic and numerical techniques it was shown that the evolution of $\mathbf{T}$, and of $\mathbf{X}$ after removing the vertical height, is $2\pi/M^2$-periodic in time. Moreover, at intermediate times that are rational multiple of $2\pi/M^2$, i.e., $t_{pq} = (2\pi/M^2)(p/q)$, with $\gcd(p, q) = 1$, the planar M-polygon evolves in such a way that it has Mq sides if q is odd, and $Mq/2$ sides if q is even, a behavior that is reminiscent of the so-called Talbot effect in optics [19, 20, 21]. Let us also mention that at a macroscopic level, effects similar to those mentioned above were also observed in the case of real fluids [22, 23].

Another interesting aspect of the evolution of the planar M-polygon is the trajectory of any of its corners, which seems to be a multifractal and resembles the graph of Riemann's non-differentiable function [24]:

$$\sum_{k=1}^{\infty} \frac{\sin(\pi k^2)}{\pi k^2}, \ t \in [0, 2]. \tag{11}$$

Recall that, for a given M, apart from the formation of new sides, the planar M-polygon evolves in the vertical direction with a constant speed c_M. Hence, bearing in mind the symmetries of the problem, the curve $\mathbf{X}(0, t)$ is planar, and after removing the vertical height from it and projecting the resulting curve onto the complex plane, it was denoted by $z_M(t)$ in [18]. Then, strong numerical evidence was given, showing that, as M tends to infinity, $z_M(t)$ converges to the complex version of Riemann's non-differentiable function:

$$\phi(t) = \sum_{k=1}^{\infty} \frac{e^{\pi i k^2 t}}{i\pi k^2}, \ t \in [0, 2]. \tag{12}$$

Recently, considering an M-sided polygon with nonzero torsion as the initial datum, new variants of $\phi(t)$ have been discovered in the trajectory $\mathbf{X}(0, t)$, whose structure depends on the torsion introduced in the problem [25]. Thus, by showing the existence of ϕ and its variants, it has been proved numerically that, in the Euclidean case, the time evolution of the smooth solutions of VFE, i.e., the circle, the helix and the straight line, is not stable. In other words, a particle can be placed on a curve arbitrarily close to a circle, helix or straight line, but, in the right topology, its trajectory converges to the graph of ϕ (or its variants). Moreover, this topology is motivated by some recent work on the well-posedness of VFE, which shows that the self-similar solutions of VFE have finite renormalized energy [26, 27].

Hence, we see that the evolution of M-sided polygons reveals many fascinating properties of VFE. With this motivation, another interesting problem could be to look at the equivalent of a planar M-polygon in the hyperbolic setting and compare the evolutions of the two. It turns out that, in the absence of torsion, the corresponding polygon is a time-like curve which is characterized by a parameter $l > 0$ representing the angle between any of its two sides. We refer to the polygonal curve as a *planar l-polygon* (alternatively, in [28], it is called an *elementary l-convex polygon*).

Note that, unlike in the Euclidean case, the planar l-polygon is open and both of its end points tend to infinity (see Figure 1). Furthermore, the corresponding tangent vector $\mathbf{T}$ lies on a unit hyperbola, and $\psi(s,0)$ is the l-periodic sum of Dirac deltas with coefficients that depend on the initial configuration of the planar l-polygon. Let us mention that, due to the mix of lack of regularity and periodicity, the well-posedness is quite challenging for this kind of problems. Recently, taking an initial datum consisting of polygonal lines that are asymptotically close to two straight lines at infinity, it has been proved that the problem is well-posed [26]. Furthermore, using the appropriate topology, in [27], it has been shown that the solution also satisfies a conservation law.

The aim of this article is twofold. First, we observe the evolution of (5)-(6) for a planar l-polygon as the initial datum (from now on, it will be referred to as the l-polygon problem). In this regard, as in the Euclidean case, the algebraic solution is obtained by working at the level of the NLS equation. However, solving the problem numerically appears to be more challenging. In particular, for our numerical simulation, as we truncate the infinitely long l-polygon, the role of boundary conditions becomes very important. Moreover, as observed in the one-corner problem, due to the exponential growth of the tangent vector, working with all the values of the parameter l becomes very difficult numerically. Bearing this in mind, we propose a numerical scheme (which will be explained in the following lines) and show a good agreement between the results thus obtained and the ones from the theoretical arguments. Then, as in [29], we answer up to what extent the l-polygon problem and the one-corner problem are related. Consequently, not only can we compute the speed of the center of mass of the planar l-polygon, but the relationship also helps in comparing the trajectory of any of the corners of a regular planar polygon in both the Euclidean and hyperbolic cases.

The structure of this article is as follows. In Section 2, we define the problem by formulating the main theoretical arguments that justify our numerical experiments. In particular, in Section 2.1, we introduce the parametric form of the initial data, and the relevant properties, such as symmetries. In Section 2.2, we observe that, as in the Euclidean case, the Galilean invariance of the NLS equation helps in obtaining the solution up to a function that depends on time. However, the function is now determined using the conservation law established for polygonal lines in [27], an approach that was also employed in [25]. Let us not forget that, in the case of curves with vanishing curvature, it is desirable to work with the parallel frame where the normal plane is spanned by vectors $\mathbf{e}_1$, $\mathbf{e}_2$ whose space derivatives depend only the $\mathbf{T}$ [30]. In the hyperbolic setting, the equivalent parallel frame is obtained as (21) where $\mathbf{e}_1$, $\mathbf{e}_2$ are the unit space-like normal and binormal vectors, respectively. With this, by integrating the generalized Frenet–Serret formulas at times that are rational multiple of $l^2/(2\pi)$, we obtain the evolution of the curve $\mathbf{X}$ and of the tangent vector $\mathbf{T}$, up to a rigid movement. This has been illustrated in Section 2.3, where knowing the rotations in the Minkowski 3-space (from now on, referred to as *hyperbolic rotations*) is found to be quite essential [31]. Moreover, the rigid movement can be determined by using the symmetries of the regular planar l-polygon and, in this way, we recover $\mathbf{T}$ completely. However, $\mathbf{X}$ is computed only up to a movement in the YZ-plane, which is obtained numerically in Section 3.2.

In Section 3, we study the numerical evolution of (5)-(6) for different values of the parameter l. Bearing in mind that, unlike in the Euclidean case, a planar l-polygon is of infinite length, we consider a planar l-polygon with only M sides in our numerical simulations, i.e., such that its length $L = lM$. We have found that Dirichlet boundary conditions on the tangent vector, with a finite difference discretization in space, combined with a fourth-order Runge-Kutta method in time, give the best numerical results, both in terms of computational cost and accuracy. These ideas have been

offered in Section 3.1. In Section 3.2, we begin by calculating the movement of the center of mass in the YZ-plane which allows us to compare the numerical solution with its algebraic counterpart (obtained in Section 2.3). On the other hand, the trajectory of a corner of the l-polygon initially located at $s = 0$, i.e., $\mathbf{X}(0, t)$, although it resembles Riemann's non-differentiable function, is quite different from its equivalent in the Euclidean case. Moreover, it converges to the function, as the parameter l tends to zero. In Section 3.2.2, we provide strong numerical evidence to prove this claim. Section 3.3 is about the behavior of the tangent vector $\mathbf{T}$ near irrational times and its comparison with the tangent vector in the Euclidean case.

Section 4 is based on the relationship between the l-polygon problem and the one-corner problem. In this regard, let us first briefly recall the main ideas of the one-corner problem. In [9], the author proves the existence of the solutions of (6) for the following initial datum

$$\mathbf{X}(s, 0) = \mathbf{A}^- s\chi_{(-\infty,0]}(s) + \mathbf{A}^+ s\chi_{[0,\infty)}(s),\ \mathbf{A}^\pm \in \mathbb{H}^2, \tag{13}$$

where, due to the rotation invariance of VFE, one can choose the unit vector $\mathbf{A}^\pm = (A_1, \pm A_2, \pm A_3)^T$. The self-similar solutions of (6) satisfying $\mathbf{X}(s, t) = \sqrt{t}\mathbf{X}(s/\sqrt{t}, 1)$, $t > 0$, solve [9, 14]

$$\frac{1}{2}\mathbf{X}(s/\sqrt{t}, 1) - \frac{s}{2\sqrt{t}}\mathbf{X}'(s/\sqrt{t}, 1) = \mathbf{X}'(s/\sqrt{t}, 1) \wedge_- \mathbf{X}''(s/\sqrt{t}, 1). \tag{14}$$

Then, from (8) and (14), one can obtain $\kappa(s, t) = c_0/\sqrt{t}$, $\tau(s, t) = s/(2t)$, where the constant c_0 characterizes the one-parameter family of smooth curves $\mathbf{X}$ that can be described using (8), $\mathbf{X}_s = \mathbf{T}$, and initial conditions

$$\begin{gathered} \mathbf{X}(0, t) = 2c_0\sqrt{t}(0, 0, 1)^T, \\ \mathbf{T}(0, t) = (1, 0, 0)^T,\ \mathbf{n}(0, t) = (0, 1, 0)^T,\ \mathbf{b}(0, t) = (0, 0, 1)^T. \end{gathered} \tag{15}$$

The parameter c_0 is the curvature of $\mathbf{X}(s, 1)$, which, in turn, is the solution of the following ODE [9]

$$\mathbf{X}'''(s, 1) + \left(-c_0^2 + \frac{s^2}{4}\right)\mathbf{X}'(s, 1) - \frac{s}{4}\mathbf{X}(s, 1) = 0. \tag{16}$$

With some abuse of notation, if we define the Fourier transform of $\mathbf{X}(s, 1)$ by

$$\hat{\mathbf{X}}(\xi) = \frac{1}{\sqrt{2\pi}}\int_{-\infty}^{\infty} \mathbf{X}(s, 1)e^{-is\xi}ds,$$

then it satisfies

$$\xi\hat{\mathbf{X}}''(\xi) + 3\hat{\mathbf{X}}'(\xi) + 4\xi^3\hat{\mathbf{X}}(\xi) + 4c_0^2\xi\hat{\mathbf{X}}(\xi) = 0. \tag{17}$$

That being said, in Section 4.1, following the approach in [29], we provide very strong numerical evidence to establish the connection between the two problems. As a consequence, in Section 4.2, an explicit expression for the speed of the center of mass of the planar l-polygon is given, according to which it moves in the vertical direction. Moreover, we also make some remarks on the trajectory of $\mathbf{X}(0, t)$.

Recall that in [9], a precise expression for the first component of the tangent vector $\mathbf{A}^\pm$ was obtained:

$$A_1 = e^{\pi c_0^2/2}, \tag{18}$$

which also relates c_0 to the time-like angle θ between $\mathbf{A}^+$ and $\mathbf{A}^-$:

$$\cosh(\theta) = -1 + 2A_1^2 = -1 + 2e^{\pi c_0^2}. \tag{19}$$

As in the Euclidean case, when $c_0 = 0$, $\theta = 0$ and $(A_1, A_2, A_3)^T = (1, 0, 0)^T$; therefore, the corresponding solution is a straight line, i.e., $\mathbf{X}(s,t) = s(1,0,0)^T$.

In Section 5.1, we rederive A_1 by means of the Laplace transform using a completely different approach. On the other hand, in Section 5.2, using the asymptotics in [9], we extract the expression for the second and third components, i.e., A_2, A_3, respectively.

Finally, in Section 6, we draw the main conclusions.

2. A solution of $\mathbf{X}_t = \mathbf{X}_s \wedge_- \mathbf{X}_{ss}$ for a planar l-polygon

One of the main aims of this article is to obtain the solutions of (6) and explain their dynamics when regular planar l-polygons are considered as initial data. In this regard, by assuming uniqueness, as in the Euclidean case, we prove the following theorem.

Theorem 1. *Assume that there exists a unique solution of the initial value problem*

$$\mathbf{X}_t = \mathbf{X}_s \wedge_- \mathbf{X}_{ss}, \tag{20}$$

with $\mathbf{X}(s,0)$ being a regular planar l-polygon. Then, at a time t_{pq} which is a rational multiple of $l^2/2\pi$, i.e., $t_{pq} \equiv (l^2/2\pi)(p/q)$, with $p \in \mathbb{Z}$, $q \in \mathbb{N}$, $\gcd(p,q) = 1$, the solution is a skew l_q-polygon with q times more sides (if q odd) or $q/2$ times more sides (if q even) in a given arc-length interval than the initial polygon. All the new sides have the same length, and the time-like angle l_q between any two adjacent sides is constant. Moreover, the polygon at a time t_{pq} is the solution of the generalized Frenet–Serret formulas

$$\begin{pmatrix} \mathbf{T}(s,t_{pq}) \\ \mathbf{e}_1(s,t_{pq}) \\ \mathbf{e}_2(s,t_{pq}) \end{pmatrix}_s = \begin{pmatrix} 0 & \alpha(s,t_{pq}) & \beta(s,t_{pq}) \\ \alpha(s,t_{pq}) & 0 & 0 \\ \beta(s,t_{pq}) & 0 & 0 \end{pmatrix} \cdot \begin{pmatrix} \mathbf{T} \\ \mathbf{e}_1 \\ \mathbf{e}_2 \end{pmatrix}, \tag{21}$$

where $\alpha(s,t_{pq}) + i\beta(s,t_{pq}) = \Psi(s,t_{pq})$, and $\Psi(s,t_{pq})$ is the l-periodic function defined over the first period $s \in [0,l)$ as

$$\Psi(s,t_{pq}) = \begin{cases} \dfrac{l_q}{\sqrt{q}} \displaystyle\sum_{m=0}^{q-1} G(-p,m,q)\delta(s - \tfrac{lm}{q}), & \text{if } q \text{ odd}, \\ \dfrac{l_q}{\sqrt{2q}} \displaystyle\sum_{m=0}^{q-1} G(-p,m,q)\delta(s - \tfrac{lm}{q}), & \text{if } q \text{ even}, \end{cases} \tag{22}$$

with

$$G(a,b,c) = \sum_{n=0}^{c-1} e^{2\pi i(an^2+bn)/c}, \ a,b \in \mathbb{Z}, c \in \mathbb{Z}\backslash\{0\},$$

being a generalized quadratic Gauss sum. The mutual time-like angle l_q between any two sides of the new polygon is given by

$$l_q = \begin{cases} 2\operatorname{arccosh}(\cosh^{1/q}(l/2)), & \text{if } q \text{ odd}, \\ 2\operatorname{arccosh}(\cosh^{2/q}(l/2)), & \text{if } q \text{ even}. \end{cases} \tag{23}$$

Let us mention that the determination of l_q is an application of the conservation law established for the polygonal lines in [27].

2.1. **Problem definition.** Given the parameter $l > 0$, an arc-length parameterized planar l-polygon can be understood as a curve with curvature given by

$$\kappa(s) = c_0 \sum_{k=-\infty}^{\infty} \delta(s - lk), \ s \in \mathbb{R}. \tag{24}$$

Here the vanishing argument of the equally spaced Dirac deltas corresponds to the location of the corners, and the coefficient $c_0 > 0$ depends on the initial configuration of the curve. In particular, bearing in mind (19), we choose

$$c_0 = \left[\frac{2}{\pi} \ln\left(\cosh\left(\frac{l}{2}\right)\right)\right]^{1/2}. \tag{25}$$

Note that, in the absence of the torsion, from (9), $\psi(s,0)$ is the curvature of the initial polygonal curve, i.e., $\psi(s,0) = \kappa(s)$, which is l-periodic. Moreover, since (5)-(6) are invariant under hyperbolic rotations, we can assume without loss of generality that the corresponding initial planar polygonal curve $\mathbf{X}(s,0)$ and its tangent vector $\mathbf{T}(s,0)$ lie on the XY-plane. Thus, writing $\mathbf{X} \equiv (X_1, X_2, X_3)^T$ and denoting the hyperbolic plane by OXY, the vertices of the planar l-polygon can be written as

$$\mathbf{X}(s_n,0) = \frac{(l/2)}{\sinh(l/2)} \left(\sinh\left(s_n\right), \cosh\left(s_n\right), 0\right)^T, \ s_n = nl, \ n \in \mathbb{Z}. \tag{26}$$

Furthermore, a point $\mathbf{X}(s,0)$, for $s_n < s < s_{n+1}$, lies in the segment that joins $\mathbf{X}(s_n,0)$ and $\mathbf{X}(s_{n+1},0)$ (see Figure 1), and the corresponding tangent vector $\mathbf{T} \equiv (T_1, T_2, T_3)^T$ is

$$\mathbf{T}(s,0) = \left(\cosh\left(l/2 + s_n\right), \sinh\left(l/2 + s_n\right), 0\right)^T, \tag{27}$$

which is piecewise constant at the interval (s_n, s_{n+1}). Note that, for our purposes, we have constructed (26), such that the vertex corresponding to $\mathbf{X}(0,0)$ lies on the y-axis. Thus, we see that

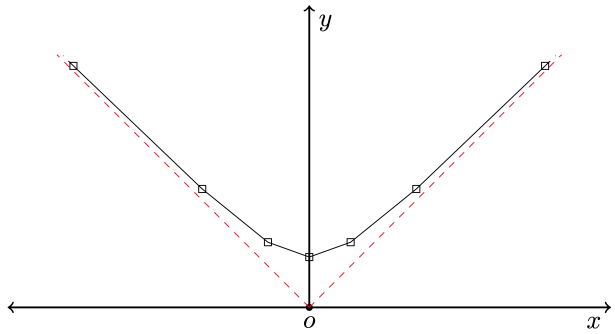

FIGURE 1. A planar l-polygon with vertices located at $s_n = nl$, $n \in \mathbb{Z}$, (black squares) and the asymptotes (dotted red lines).

$\mathbf{X}(s,0)$ is a curve with infinite length; however, since one of the main concerns in this article is to address the numerical evolution of a planar l-polygon, we need to work with a finite curve. In this respect, without loss of generality, taking the number of sides M to be even, we consider a planar

l-polygon with vertices located at

$$\mathbf{X}(s_n,0)=\frac{(l/2)}{\sinh(l/2)}\left(\sinh(s_n),\cosh(s_n)-\frac{\sinh(L/2)}{M\tanh(l/2)},0\right)^T, \tag{28}$$

where $s_n=-L/2+nl$, $n=0,1,2,\dots,M$, and $L=lM$ is its length. The corresponding tangent vectors $\mathbf{T}$ are the same as in (27).

2.1.1. *Spatial symmetries of* $\mathbf{X}$ *and* $\mathbf{T}$. The invariance of (5)-(6) under hyperbolic rotations follows from that of the Minkowski cross product under them [31]. Thus, given a hyperbolic rotation matrix $\mathbf{R}$ such that $\mathbf{R}\cdot\mathbf{T}(s,0)=\mathbf{T}(s,0)$ and $\mathbf{R}\cdot\mathbf{X}(s,0)=\mathbf{X}(s,0)$, if the solution is unique, then $\mathbf{R}\cdot\mathbf{X}(s,t)=\mathbf{X}(s,t)$, $\mathbf{R}\cdot\mathbf{T}(s,t)=\mathbf{T}(s,t)$, for all t. In particular, since $\mathbf{X}(s,0)$ and $\mathbf{T}(s,0)$, which are given respectively by (26) and (27), are invariant under a rotation of time-like angle nl about a space-like z-axis for all $n\in\mathbb{Z}$, it can be concluded that $\mathbf{X}(s,t)$ and $\mathbf{T}(s,t)$ are invariant under hyperbolic rotations, for all t.

One important consequence of these symmetries is that, for any time t, $\mathbf{X}(s+nl,t)$ always lies in the same orthogonal plane to the z-axis. Furthermore, as in the Euclidean case, (5)-(6) are mirror invariant, and, consequently, $\mathbf{X}(s,t)-\mathbf{X}(-s,t)$ is a positive multiple of $(1,0,0)^T$. This property plays an important role when constructing the algebraic solutions.

2.2. **Problem formulation and the behavior at rational multiples of the time period.** Let us first mention that at the level of the NLS equation, the hyperbolic case is not much different from the Euclidean case; however, the obtention of $\mathbf{T}$ and $\mathbf{X}$ depends entirely on hyperbolic rotations [31, 5]. In this regard, following the approach in [18], we observe that, by definition, $\psi(s,0)$ is l-periodic, and, since (10) is invariant with respect to space translations, $\psi(s,t)$ is also l-periodic for all $t\in\mathbb{R}$. On the other hand, $\psi(s,0)=e^{irks}\psi(s,0)$, $r=2\pi/l$, $l>0$; thus, from the Galilean invariances of (10), $\psi(s,t)=e^{irks-i(rk)^2t}\psi(s-2rkt,t)$, for all k. Furthermore, since ψ is periodic, using its Fourier coefficients, it can be expressed as

$$\psi(s,t)=\hat{\psi}(0,t)\sum_{k=-\infty}^{\infty}e^{i(rk)^2t+i(rk)s}, \tag{29}$$

where $\hat{\psi}(0,t)$ is a constant depending on time t. Due to the gauge invariance, we can take it to be real (see [18]), and its value is computed explicitly by using a conservation law that will be explained in the following lines. Remark that $\psi(s,t)$ is periodic in time with period $2\pi/r^2$, or, $l^2/2\pi$, which we denote by T_f in this paper.

Next, evaluating (29) at rational multiples of the time period T_f, i.e., at $t=t_{pq}=\frac{2\pi}{r^2}\frac{p}{q}$, $p\in\mathbb{Z}, q\in\mathbb{N}$, $\gcd(p,q)=1$, gives (See [18, Section 3.3] for the intermediate steps):

$$\psi(s,t_{pq})=\begin{cases}\dfrac{l}{\sqrt{q}}\hat{\psi}(0,t_{pq})\displaystyle\sum_{m=0}^{q-1}e^{i\theta_m}\delta\left(s-\tfrac{ml}{q}\right), & \text{if } q \text{ odd},\\[2ex] \dfrac{l}{\sqrt{q/2}}\hat{\psi}(0,t_{pq})\displaystyle\sum_{m=0}^{q/2-1}e^{i\theta_{2m+1}}\delta\left(s-\tfrac{(2m+1)l}{q}\right), & \text{if } q/2 \text{ odd},\\[2ex] \dfrac{l}{\sqrt{q/2}}\hat{\psi}(0,t_{pq})\displaystyle\sum_{m=0}^{q/2-1}e^{i\theta_{2m}}\delta\left(s-\tfrac{2ml}{q}\right), & \text{if } q/2 \text{ even},\end{cases} \tag{30}$$

for $s \in (0, l)$. This implies that, at any rational time t_{pq}, a single side of the l-polygon at $t = 0$ will evolve into q sides if q is odd, and $q/2$ sides if q is even. Since it holds true for any $k \in \mathbb{Z}$, this would imply that the resulting polygon will have q or $q/2$ times more sides than the initial l-polygon. The new Dirac deltas thus formed are equally spaced and, as a result, all the sides of the new polygon are of equal length. Furthermore, the coefficients of Dirac deltas have equal modulus and are given by

$$c_q = \begin{cases} \frac{l}{\sqrt{q}}\hat{\psi}(0, t_{pq}), & \text{if } q \text{ is odd,} \\ \frac{l}{\sqrt{q/2}}\hat{\psi}(0, t_{pq}), & \text{if } q \text{ is even.} \end{cases}$$

Note that the conservation law established for the polygonal lines in [27] holds true for both the focusing and the defocusing NLS equation. Therefore, by following the approach in [25], we obtain $c_q = c_0/\sqrt{q}$, if q is odd, and $c_q = c_0/\sqrt{2q}$, if q is even, and

$$\hat{\psi}(0, t_{pq}) = c_0/l. \tag{31}$$

On the other hand, (25) holds true whenever a corner is created, for instance, in our case, at rational times t_{pq}. Then, by recalling (19) and denoting the time-like angle between any two tangent vectors by l_q, we have

$$\cosh\left(\tfrac{l_q}{2}\right) = e^{\pi c_q^2/2}. \tag{32}$$

Moreover, since c_q is independent from k, the angle l_q is the same for all sides and, thus, using (25), (31), (32) it can be expressed as

$$l_q = \begin{cases} 2\,\mathrm{arccosh}(\cosh^{1/q}(l/2)), & \text{if } q \text{ odd,} \\ 2\,\mathrm{arccosh}(\cosh^{2/q}(l/2)), & \text{if } q \text{ even.} \end{cases} \tag{33}$$

2.3. **Algebraic solution.** In order to construct the algebraic solution, as in [18], we integrate the Frenet–Serret formulas (21), taking

$$\Psi(s, t_{pq}) = \frac{l_q}{c_q}\psi(s, t_{pq}) = \alpha(s, t_{pq}) + i\beta(s, t_{pq}), \tag{34}$$

for q odd, and similarly for q even. Then, by expressing $\alpha + i\beta = l_q e^{i\theta}$, the integration yields

$$\mathbf{H} = \begin{pmatrix} \cosh(l_q) & \cos(\theta)\sinh(l_q) & \sin(\theta)\sinh(l_q) \\ \cos(\theta)\sinh(l_q) & 1 + \cos^2(\theta)(\cosh(l_q) - 1) & \sin(\theta)\cos(\theta)(\cosh(l_q) - 1) \\ \sin(\theta)\sinh(l_q) & \sin(\theta)\cos(\theta)(\cosh(l_q) - 1) & 1 + \sin^2(\theta)(\cosh(l_q) - 1) \end{pmatrix}, \tag{35}$$

which is a hyperbolic rotation of angle l_q about a space-like axis $(0, -\sin(\theta), \cos(\theta))^T$ [31]. In other words, $\mathbf{H}$ describes the transition from a vertex located at $s_k = -L/2 + k(l/q)$, $k = 0, 1, \ldots, Mq - 1$. By choosing the basis vectors $\tilde{\mathbf{T}}(s)$, $\tilde{\mathbf{e}}_1(s)$, $\tilde{\mathbf{e}}_2(s)$, such that they form an identity matrix at $s = s_0^-$, we obtain their values for the remaining Mq sides by a subsequent action of $\mathbf{H}$ corresponding to $\Psi(s, t_{pq})$. Additionally, $\tilde{\mathbf{X}}$, i.e., $\mathbf{X}$ up to a rigid movement, can be computed from $\tilde{\mathbf{T}}$ through

$$\tilde{\mathbf{X}}(s_{k+1}) = \tilde{\mathbf{X}}(s_k) + \tfrac{l}{q}\tilde{\mathbf{T}}(s_k^+), \;\; k = 0, 1, \ldots, Mq, \tag{36}$$

where $\tilde{\mathbf{X}}(s_0)$ can be assigned any value, for example, $\tilde{\mathbf{X}}(s_0) = (0, 0, 0)^T$.

Next, we determine the correct rotation by using the symmetries of the regular planar l-polygon. First, in order to align the polygon orthogonal to the z-axis, we use the fact that at any time t,

$\mathbf{X}(lk)$, lies in the XY-plane, for $k \in \mathbb{Z}$. Then, the resulting curve is rotated about the z-axis in such a way that $\mathbf{X}(l) - \mathbf{X}(-l)$ is a positive multiple of $(1,0,0)^T$. This can be done efficiently in the following way:

(1) Compute the unit time-like vectors $\mathbf{w}^+ = \frac{\tilde{\mathbf{X}}(l)-\tilde{\mathbf{X}}(0)}{|\tilde{\mathbf{X}}(l)-\tilde{\mathbf{X}}(0)|_0}$, $\mathbf{w}^- = \frac{\tilde{\mathbf{X}}(-l)-\tilde{\mathbf{X}}(0)}{|\tilde{\mathbf{X}}(-l)-\tilde{\mathbf{X}}(0)|_0}$.
(2) Compute the unit space-like vector $\hat{\mathbf{u}} = \frac{\mathbf{w}^+ \wedge_- \mathbf{w}^-}{|\mathbf{w}^+ \wedge_- \mathbf{w}^-|_0}$.
(3) If the space-like vectors $\hat{\mathbf{u}}$ and $\hat{\mathbf{z}} = (0,0,1)^T$ are such that [5]:
   (a) $(\hat{\mathbf{u}})_3 > |\hat{\mathbf{u}}|_0$, then the time-like angle $\nu_1 = \operatorname{arccosh}((\hat{\mathbf{u}})_3/|\mathbf{u}|_0)$, and $\hat{\mathbf{v}} = \hat{\mathbf{u}} \wedge_- \hat{\mathbf{z}}$ is a space-like vector,
   (b) $(\hat{\mathbf{u}})_3 < |\hat{\mathbf{u}}|_0$, then the space-like angle $\nu_1 = \arccos((\hat{\mathbf{u}})_3/|\mathbf{u}|_0)$, and $\hat{\mathbf{v}} = \hat{\mathbf{u}} \wedge_- \hat{\mathbf{z}}$ is a time-like vector,
   (c) $(\hat{\mathbf{u}})_3 = |\hat{\mathbf{u}}|_0$, then $\nu_1 = 0$, and $\mathbf{L}_1$ is an identity matrix, then, $\mathbf{L}_1$ is a matrix performing a rotation of an angle ν_1 about the axis $\hat{\mathbf{v}}/|\hat{\mathbf{v}}|_0$ [31].
(4) Compute time-like vectors $\mathbf{w}^+_{rot} = \mathbf{L}_1 \cdot \mathbf{w}^+$, $\mathbf{w}^-_{rot} = \mathbf{L}_1 \cdot \mathbf{w}^-$, and $\mathbf{w} = \frac{\mathbf{w}^+_{rot}-\mathbf{w}^-_{rot}}{|\mathbf{w}^+_{rot}-\mathbf{w}^-_{rot}|_0}$. Then, $\nu_2 = \operatorname{arccosh}(\mathbf{w} \circ_- (1,0,0)^T)$ is the time-like angle, and $\mathbf{L}_2$ is the corresponding rotation about the axis given by $\frac{\mathbf{w}\wedge_-(1,0,0)}{|\mathbf{w}\wedge_-(1,0,0)|_0}$.
(5) Compute the desired rotation $\mathbf{L} = \mathbf{L}_2 \cdot \mathbf{L}_1$, and $\mathbf{T} = \mathbf{L} \cdot \tilde{\mathbf{T}}$, $\mathbf{X} = \mathbf{L} \cdot \tilde{\mathbf{X}}$.

Thus, we obtain $\mathbf{X}$, $\mathbf{T}$ correctly oriented. Although, the computation of $\mathbf{T}$ is complete, in order to determine $\mathbf{X}$ completely, we need to compute the movement of its center of mass which is done in the next section. Finally, from (30), (31) and (34), we conclude the proof of Theorem 1.

3. Numerical solution

As mentioned previously, in order to compute the numerical evolution, we consider an l-polygon of length L that is now characterized by two parameters l and M, such that $L = l \cdot M$. For our purposes, we take M even, so the initial curve $\mathbf{X}(s,0)$, $s \in [-L/2, L/2]$, has a vertex located at $s = 0$ and the symmetries described in Section 2.1.1 apply. This also allows us to capture the time evolution of a corner initially located at $s = 0$, i.e., $\mathbf{X}(0,t)$. Furthermore, with M, we approximate an infinitely long polygon; evidently, more accurate results are obtained with a large value of L. However, for a fixed M, due to the exponential growth of the Euclidean norm of the tangent vector $\mathbf{T}$, a large value of l causes the solution to blow up in a short time, making the numerical scheme unstable. This was also observed in the one-corner problem, where a large value of c_0 leads to similar effects [15]. On the other hand, a large value of M restricts us to consider only small values of l. Let us not forget that, since we are truncating the l-polygon, the role of the boundary conditions is also very important.

Our goal is to solve (5)-(6) numerically for the initial data given by (27)-(28), for $s \in [-L/2, L/2]$. There have been several papers dedicated to the numerical treatment of (5)-(6) [14, 15, 18]. For instance, in a recent work on the Euclidean regular M-polygons, the coupled system is solved with a pseudo-spectral method in space and a fourth-order Runge-Kutta method in time [18, 25]. In our case, a Chebyshev spectral discretization with an explicit scheme in time poses a severe restriction $|\Delta t| = \mathcal{O}(1/N^4)$, where N is the number of nodes. On the other hand, due to its low order of accuracy, a second-order semi-implicit backward difference formula applied on the stereographic projection of (5) does not serve our needs, unlike in [15]. As a result, after trying several numerical

methods, we are convinced that both in terms of efficiency and computational cost, a fourth-order finite difference discretization in space combined with a fourth-order Runge-Kutta method in time and fixed boundary conditions on $\mathbf{T}$ yields the best results.

3.1. **Numerical method.** We divide the interval $[-L/2, L/2]$ into $N+1$ equally spaced nodes $s_j = -L/2 + jL/N,\ j = 0, 1, \ldots, N$, with a step size $\Delta s = L/N$. The time interval $[0, T_f]$ has been discretized into $N_t + 1$ equally spaced time steps $t_n = n\Delta t,\ n = 0, 1, \ldots, N_t$, with $\Delta t = T_f/N_t$. We denote $\mathbf{X}_j^{(n)} \equiv \mathbf{X}^{(n)}(s_j) \equiv \mathbf{X}(s_j, t_n)$, where $\mathbf{X}_j^{(0)}$ can be computed from (28) by using linear interpolation, and $\mathbf{T}_j^{(n)} \equiv \mathbf{T}^{(n)}(s_j) \equiv \mathbf{T}(s_j, t_n)$, where $\mathbf{T}(s_j, \cdot) = \mathbf{T}(s, \cdot)$, for $s_j \leq s < s_{j+1}$, if $s < 0$, and $s_j < s \leq s_{j+1}$, if $s > 0$. Thus, we obtain N values of the piecewise constant tangent vector, each corresponding to N segments, respectively.

Furthermore, in order to approximate the first and second derivatives, we use a fourth-order central difference scheme for the inner points, and, to keep the same order of accuracy over all the discretized domain, we employ a fourth-order forward/backward difference scheme for the boundary and its neighboring points. As a result, we obtain banded differentiation matrices of size $(N+1) \times (N+1)$. Let us mention that, in order to maintain the dimensions of the vectors $\mathbf{X}_j^{(n)}$ and $\mathbf{T}_j^{(n)}$ consistent, we obtain the $N+1$ values of the piecewise continuous tangent vector $\mathbf{T}_j^{(0)}$ in the following way:

$$\tilde{\mathbf{T}}_0^{(0)} = \mathbf{T}_0^{(0)},\ \tilde{\mathbf{T}}_{j+1}^{(0)} = (\mathbf{T}_j^{(0)} + \mathbf{T}_{j+1}^{(0)})/2,\ j = 0, 1, \ldots, N-2,$$
$$\tilde{\mathbf{T}}_N^{(0)} = \mathbf{T}_{N-1}^{(0)},\ \mathbf{T}_j^{(0)} = \tilde{\mathbf{T}}_j/|\tilde{\mathbf{T}}_j|_0.$$

Hence, by fixing the boundary conditions for the tangent vector $\mathbf{T}$, which can be introduced explicitly, we solve the following initial-boundary value problem:

$$\begin{cases} \mathbf{T}_t(s,t) = \mathbf{T}(s,t) \wedge_- \mathbf{T}_{ss}(s,t), \\ \mathbf{X}_t(s,t) = \mathbf{X}_s(s,t) \wedge_- \mathbf{X}_{ss}(s,t) = \mathbf{T}(s,t) \wedge_- \mathbf{T}_s(s,t), \\ \mathbf{T}(-L/2,t) = (\cosh(l/2 - L/2), \sinh(l/2 - L/2), 0)^T, \\ \mathbf{T}(+L/2,t) = (\cosh(l/2 + L/2), \sinh(l/2 + L/2), 0)^T,\ t \in [0, T_f], \end{cases} \tag{37}$$

with initial conditions $\mathbf{X}(s,0)$, $\mathbf{T}(s,0)$ given by (27), (28), respectively. By using the space discretization mentioned above, we integrate (37) numerically by means of a fourth-order Runge-Kutta method in time. Moreover, in the numerical implementation, at the end of each time step t_n, we renormalize the tangent vector, so that $\mathbf{T}^{(n)} \in \mathbb{H}^2$.

To determine the stability constraints of the numerical scheme, we compute the maximum value of the time step Δt for which the solution does not blow up. Thus, giving different values to the parameters N, M, l we obtain $\Delta t/\Delta s^2 \approx 0.5302$, i.e., $\Delta t = \mathcal{O}(\Delta s^2)$.

Let us remark that, in the case of a planar M-polygon, the space derivatives could be approximated at N nodes by using the `fft` algorithm in MATLAB. Moreover, due to the symmetries of the tangent vector, this could be done using only one side of the M-polygon; thus, with a computation cost $\mathcal{O}((N/M)\log(N/M))$ [18]. However, in the current scenario, due to the fixed boundary conditions, we work with all the sides of the truncated l-polygon, and, therefore, the space derivatives are approximated with finite difference matrices of size $(N+1) \times (N+1)$. Hence, achieving the same level of accuracy would be very expensive computationally.

3.2. **Numerical results.** Recall that, given any rational time, the computation of algebraic solutions, which we call $\mathbf{T}_{alg}$, $\mathbf{X}_{alg}$, is entirely based on the assumption of uniqueness. In the following lines, we will see that, up to some numerical errors, the numerical solutions, denoted by $\mathbf{X}_{num}$, $\mathbf{T}_{num}$, match very well the ones obtained from theoretical arguments. However, remark that, in order to compare the two solutions, we need to specify the movement of $\mathbf{X}_{alg}$ at any rational time. This is done by computing the center of mass, which is given by the mean of $\mathbf{X}$, i.e.,

$$\mathbf{X}^{mean}(t) = \frac{1}{L}\int_{-L/2}^{L/2} \mathbf{X}(s,t)ds.$$

Thus, with the discretization mentioned above, we approximate the integral numerically using the trapezoidal rule. Having the aim to analyze $\mathbf{X}^{mean}$ componentwise, we note that the first component is equal to zero, from the symmetries mentioned in Section 2.1.1; moreover, denoting the second and third components by $X_{2,0}^{mean}$ and $X_{3,0}^{mean}$, respectively, we have

$$X_{2,0}^{mean}(t) = \frac{1}{N}\sum_{j=0}^{N-1} X_2(s_j,t),\ X_{3,0}^{mean}(t) = \frac{1}{N}\sum_{j=0}^{N-1} X_3(s_j,t). \tag{38}$$

Let us mention that $X_{3,0}^{mean}$ describes the position of the center of mass along the z-axis, i.e., the vertical height of the polygonal curve $\mathbf{X}$. After performing numerical simulations for different values of M and l, we observe that $X_{3,0}^{mean}(t)$ can be very well approximated by means of a constant multiplied by t. To be precise,

$$X_{3,0}^{mean}(t) \approx \frac{X_{3,0}^{mean}(T_f)}{T_f} t = c_l^{num}\ t, \tag{39}$$

where c_l^{num} is the mean speed computed numerically, and its exact value will be given as a consequence of Theorem 2.

On the other hand, we find that the values of $\mathbf{T}_{num}$ (and, hence, those of $\mathbf{X}_{num}$) corresponding to the inner grid points are far more accurate than the ones close to the boundary. For instance, on the left-hand side of Figure 2, we show the comparison between the third component of $\mathbf{T}_{alg}$ and $\mathbf{T}_{num}$ for $M = 96$, $l = 0.1$, $N/M = 2^9$, $s \in [-L/2, L/2]$. The reason behind this is clearly the exponential growth of the tangent vector near the boundary, and the fact that we are approximating piecewise continuous functions using a finite difference scheme. As a result, for a better approximation of $\mathbf{X}^{mean}$, we choose to work with the inner points of the discretized domain. To make a reasonable choice of the "inner points", we define

$$X_{3,r}^{mean}(t) = \frac{1}{N_r}\sum_{j=2rN/M}^{N-2rN/M-1} X_3(s_j,t),\ r = 0,1,\dots,M/4-1, \tag{40}$$

for $N_r = N-(4rN/M)$, i.e., the mean of $X_3(s_j,t)$ for $s_j \in [-L/2+2rl, L/2-2rl]$. Then, for each r, we compute the maximum difference between $X_{3,r}^{mean}(t)$ and its exact linear approximation $c_l t$, i.e., $\max_n(|X_{3,r}^{mean}(t^{(n)}) - c_l t^{(n)}|)$. The right-hand side of Figure 2 clearly shows that the error is smaller when the nodes closer to the boundary are avoided. It also shows that, after certain values of r, the error does not vary much. Thus, without loss of generality, we can take $r = M/8$, which implies $s_j \in [-L/4, L/4]$, i.e., $j = N/4+1, N/4+2, \dots, 3N/4$. Note that, although using the symmetries,

$X_{3,0}^{mean}(t^{(n)})$ can be computed using only N/M values, due to the unevenness of errors discussed above, we prefer to use $N/2$ elements.

In order to further strengthen the claim of (39), we compute $\max_n(|X_{3,r}^{mean}(t^{(n)}) - c_l t^{(n)}|)$, for different values of l and a fixed r. Since a regular planar l-polygon is characterized by the parameter l, the speed of center of mass depends only on it; however, we are approximating the infinitely long l-polygon with the parameter M, and, as a consequence, better results are obtained for larger values of M. Therefore, in our simulations, we have taken a moderately large value, i.e., $M = 96$, and different values of l and N/M. Table 1 displays the corresponding errors, and it is clear that whenever the number of grid points is doubled, the error decreases by a factor slightly lower than two, hence suggesting a convergence of the order of $\mathcal{O}((N/M)^{-1})$. The table also shows the value of $c_l - 1$ for each l, because c_l is very close to 1. Clearly, c_l converges to 1, as l goes to zero, i.e., $\mathbf{X}(s, 0)$ tends to a hyperbola.

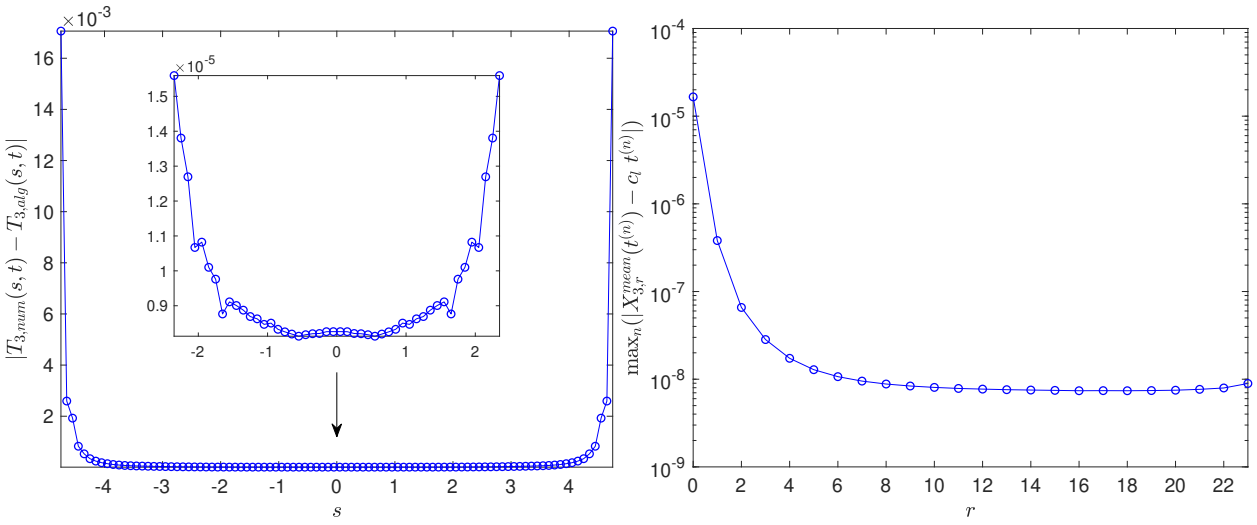

FIGURE 2. Left: $|T_{3,num}(s,t) - T_{3,alg}(s,t)|$, at $t = T_f$, for $M = 96$, $l = 0.1$, $N/M = 2^9$, $s \in [-L/2, L/2]$, where the values represented by blue circles are computed using the mean of N/M values for each side. Right: $\max_n(|X_{3,r}^{mean}(t^{(n)}) - c_l t^{(n)}|)$, where the mean of $X_3(s_j, t^{(n)})$ has been computed using $4rN/M$ values, such that $s_j \in [-L/2 + 2rl, L/2 - 2rl]$, $r = 0, 1, 2, \ldots, M/4 - 1$, $c_l = 1.000416458444891$. Clearly, the errors are much lower when the inner points are considered.

Furthermore, it is possible to approximate $\mathbf{X}^{mean}$ using also the algebraic solution, so the numerical errors can be avoided completely. Using the approach in [29, Section 4], we compute it as

$$\mathbf{X}^{mean}(t) = \int_0^t \text{mean}(\mathbf{X}_t)(t')dt' = \int_0^t \left[\frac{1}{L}\int_{-L/2}^{L/2} \mathbf{X}_t(s,t')ds\right] dt'. \tag{41}$$

l	$N/M = 2^6$	$N/M = 2^7$	$N/M = 2^8$	$N/M = 2^9$	$(c_l - 1)$
0.15	$2.0578 \cdot 10^{-7}$	$1.1334 \cdot 10^{-7}$	$6.3398 \cdot 10^{-8}$	$3.7051 \cdot 10^{-8}$	$9.3645 \cdot 10^{-4}$
0.12	$8.4311 \cdot 10^{-8}$	$4.6133 \cdot 10^{-8}$	$2.6124 \cdot 10^{-8}$	$1.5543 \cdot 10^{-8}$	$5.9957 \cdot 10^{-4}$
0.1	$4.0669 \cdot 10^{-8}$	$2.2237 \cdot 10^{-8}$	$1.2801 \cdot 10^{-8}$	$7.7110 \cdot 10^{-9}$	$4.1646 \cdot 10^{-4}$
0.05	$2.5460 \cdot 10^{-9}$	$1.5103 \cdot 10^{-9}$	$9.2425 \cdot 10^{-10}$	$6.1407 \cdot 10^{-10}$	$1.0415 \cdot 10^{-4}$
0.025	$1.6008 \cdot 10^{-10}$	$1.2481 \cdot 10^{-10}$	$8.8786 \cdot 10^{-11}$	$7.1406 \cdot 10^{-11}$	$2.6040 \cdot 10^{-5}$

TABLE 1. $\max_n(|X^{mean}_{3,r}(t^{(n)}) - c_l t^{(n)}|)$, for $M = 96$ and different N/M, l and corresponding values of c_l, where $X^{mean}_{3,r}(t^{(n)})$ is computed using (40), for $r = M/8$.

Thus, for any rational time t_{pq}, the first integral is precisely given by

$$\int_{-L/2}^{L/2} \mathbf{X}_t(s, t_{pq}) ds = \frac{l_q}{\sinh(l_q)} \sum_{k=0}^{Mq-1} \mathbf{T}_{alg,k} \wedge_- \mathbf{T}_{alg,k+1}, \tag{42}$$

where $\mathbf{T}_{alg,k} = \mathbf{T}_{alg}(s_k^+, \cdot)$, and, with a large q, the integral with respect to time in (41) can be approximated with a third-order method. In this regard, we have taken $M = 8$, $l = 0.6$, $q = 7560$ and the interval $[0, T_f]$ has been divided into q equally spaced segments. We have plotted the integral in (42), whose first component is zero and the other two seem to have a very oscillatory behavior (see the first two plots in Figure 3). However, after integrating in time, the oscillations disappear and we obtain the components of $\mathbf{X}^{mean}$, where the second component is periodic and the third component is a straight line whose slope converges to c_l with q.

3.2.1. *Comparison between numerical and algebraic solutions.* Having understood the movement of the center of mass of $\mathbf{X}$, we remove it from $\mathbf{X}_{num}$, and then compare it with $\mathbf{X}_{alg}$. Recall that, from the algebraic solution we know the vertices $\mathbf{X}_{alg}$, so the non-vertex values have been computed using linear interpolation. Thus, we calculate $\max_{j,n}(\|\mathbf{X}_{num}(s_j, t^{(n)}) - (0, X^{mean}_{2,r}(t^{(n)}), c_l\ t^{(n)}) - \mathbf{X}_{alg}(s_j, t^{(n)})\|)$, where $\|\cdot\|$ is the Euclidean norm. On the other hand, given the size of the discretization, it is computationally very difficult to compare the solutions at all the $N_t + 1$ time instants; therefore, we do it for a fairly large amount, for example, $N_t = 1260$.

Continuing as in the previous section, in Table 3.2.1, we show the errors for $M = 48$ and different values of l and N/M, and $r = M/8$, i.e., $N/2+1$ inner points, which decrease according to a certain factor, as the discretization is made finer. Moreover, the error when $r = 0$, i.e., we consider all the $N + 1$ points, is of the order of $\mathcal{O}(10^{-1})$, for $l = 0.2$, $N/M = 2^{10}$, and decreases to the order of $\mathcal{O}(10^{-2})$, for $l = 0.025$, using the same discretization. Although the convergence is slow, bearing in mind that $\max \|\mathbf{X}_{alg}\| \gg 1$, the results are satisfactory and show that, as N grows larger, the numerical solution converges to the algebraic one. It also gives strong evidence that, up to the vertical height, the evolution of $\mathbf{X}$ is T_f-periodic in time.

On the other hand, Figure 5 shows $T_{1,num}$, the first component of the tangent vector, at different rational times. From the magnified part, it is quite clear that, at half the time period, the tangent vector is continuous at $s = 0$, i.e., there is no corner at that time; moreover, the oscillations causing the errors are more prominent toward the boundary. At the end of one time period, up to the numerical errors, it matches the tangent vector at initial time, thus showing the time periodicity of $\mathbf{T}_{num}$ (in yellow). Figure 4 shows all the three components of the tangent vector for both the

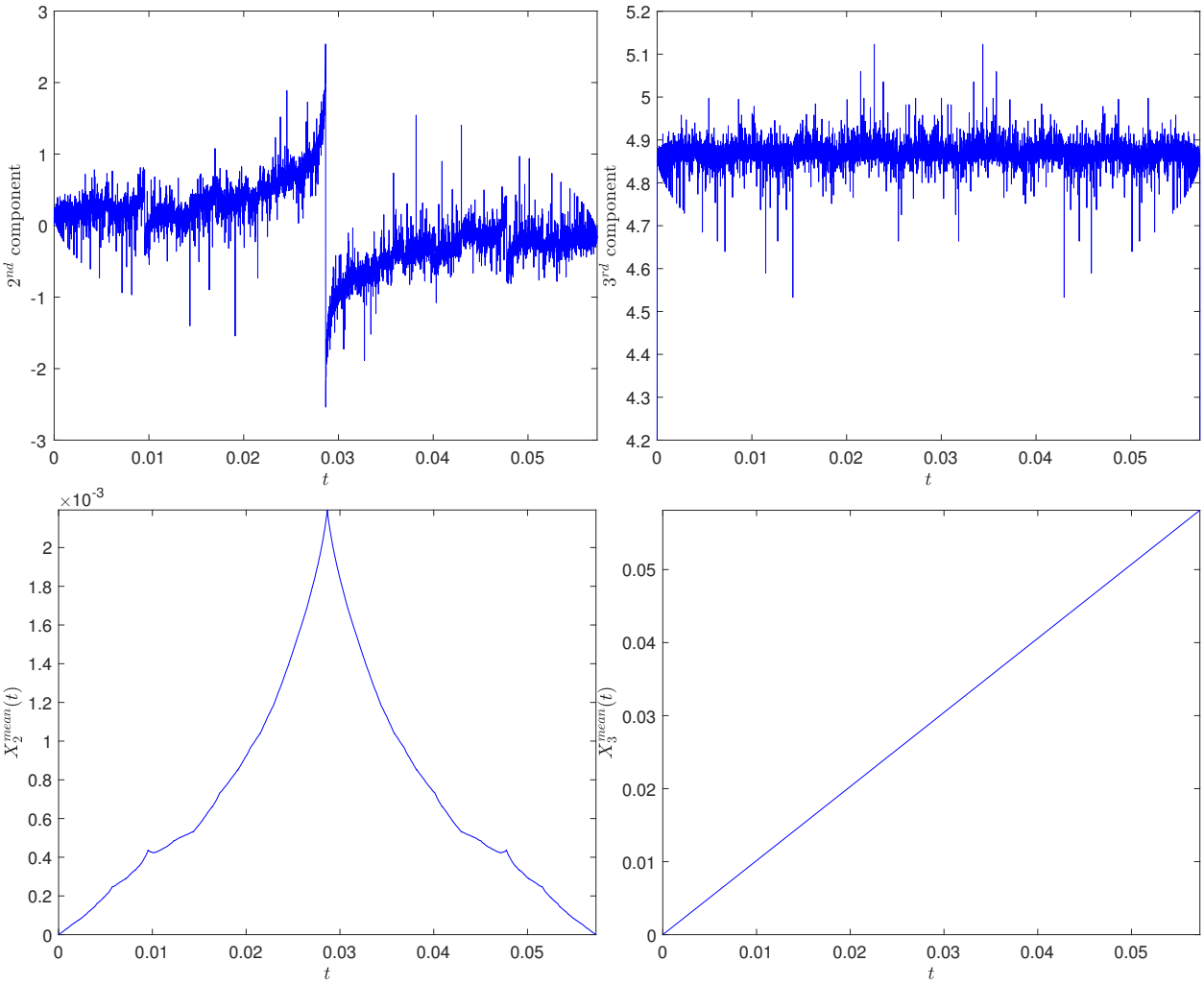

FIGURE 3. Second and third components of (41) and (42), computed for $M = 8$, $l = 0.6$, $q = 7560$. Integrating with respect to time, the oscillations clearly disappear, and we obtain a periodic curve and a straight line, respectively.

numerical and the algebraic solutions, at one third of the time period. One can clearly see that there are three times more segments and, apart from the numerical oscillations, the two figures are similar. For $M = 48$, at $t = t_{1,3}$, the tangent vector takes $Mq = 144$ different values:

$$\mathbf{T}_{alg,1} = \begin{pmatrix} 6.0854 \cdot 10^1 \\ -6.0846 \cdot 10^1 \\ -5.7735 \cdot 10^{-2} \end{pmatrix}, \ \mathbf{T}_{alg,2} = \begin{pmatrix} 5.4978 \cdot 10^1 \\ -5.4969 \cdot 10^1 \\ 0 \end{pmatrix}, \ \mathbf{T}_{alg,3} = \begin{pmatrix} 4.9836 \cdot 10^1 \\ -4.9825 \cdot 10^1 \\ 5.7735 \cdot 10^{-2} \end{pmatrix}, \tag{43}$$

and the rest of them can be computed, applying consecutively a hyperbolic rotation of a time-like angle l about a space-like z-axis in the counter-clockwise direction. For instance, the values of the

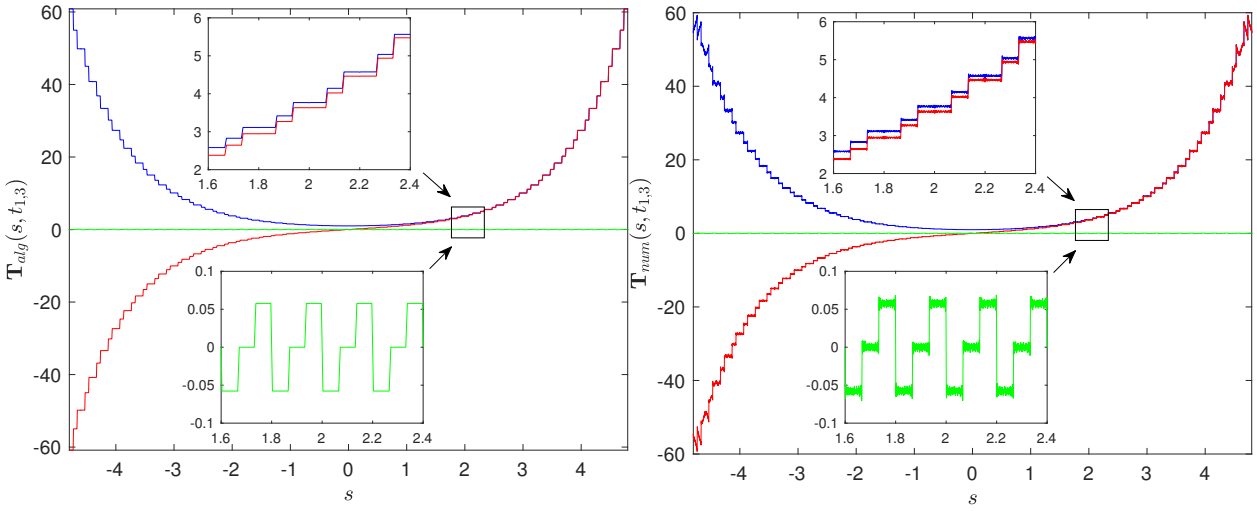

FIGURE 4. $\mathbf{T}_{num}(s,t)$ (left) and $\mathbf{T}_{alg}$ (right) at $t = t_{1,3}$ $l = 0.2$, $M = 48$, $N/M = 2^{11}$.

tangent vector at $s = 0^-$ are obtained by a hyperbolic rotation of angle $L/2 - l$ about the z-axis:

$$\mathbf{T}_{alg,70} = \begin{pmatrix} 1.0217 \\ -2.0156 \cdot 10^{-1} \\ -5.7735 \cdot 10^{-2} \end{pmatrix}, \mathbf{T}_{alg,71} = \begin{pmatrix} 1.0050 \\ -1.0017 \cdot 10^{-1} \\ 0 \end{pmatrix}, \mathbf{T}_{alg,72} = \begin{pmatrix} 1.0017 \\ -1.1093 \cdot 10^{-4} \\ 5.7735 \cdot 10^{-2} \end{pmatrix}. \quad (44)$$

In order to compare them with the corresponding numerical solution, we take the mean of each

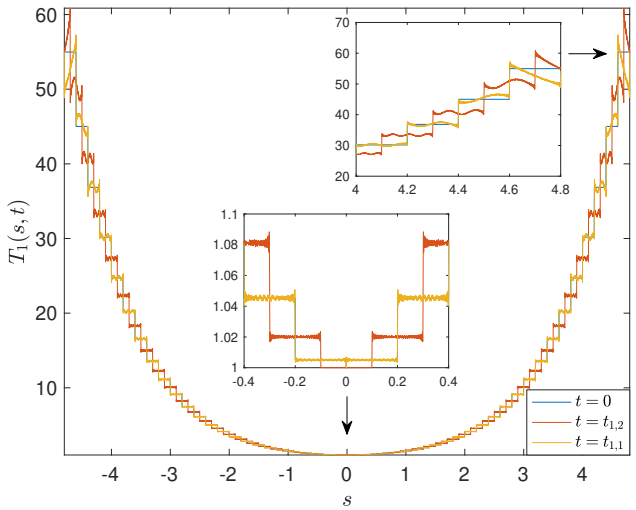

FIGURE 5. The first component of $\mathbf{T}_{num}(s,t)$ for $M = 48$, $l = 0.2$, $N/M = 2^{11}$, at initial time, final time and half the time period.

segment and compute the absolute difference. Thus, with a discretization given by $N/M = 2^{11}$, the maximum absolute and relative errors taking (43) are of the order of $\mathcal{O}(1)$, $\mathcal{O}(10^{-1})$, and, taking

l	$N/M = 2^6$	$N/M = 2^7$	$N/M = 2^8$	$N/M = 2^9$	$N/M = 2^{10}$
0.2	$4.0442 \cdot 10^{-2}$	$3.2678 \cdot 10^{-2}$	$2.6665 \cdot 10^{-2}$	$2.2341 \cdot 10^{-2}$	$1.9248 \cdot 10^{-2}$
0.15	$2.2711 \cdot 10^{-2}$	$1.8066 \cdot 10^{-2}$	$1.4479 \cdot 10^{-2}$	$1.1974 \cdot 10^{-2}$	$1.0171 \cdot 10^{-2}$
0.12	$1.5620 \cdot 10^{-2}$	$1.2359 \cdot 10^{-2}$	$9.8698 \cdot 10^{-3}$	$8.4188 \cdot 10^{-3}$	$7.2017 \cdot 10^{-3}$
0.1	$1.1894 \cdot 10^{-2}$	$9.3896 \cdot 10^{-3}$	$7.5154 \cdot 10^{-3}$	$6.4954 \cdot 10^{-3}$	$5.5810 \cdot 10^{-3}$
0.05	$5.0056 \cdot 10^{-3}$	$3.9380 \cdot 10^{-3}$	$3.2342 \cdot 10^{-3}$	$2.8058 \cdot 10^{-3}$	$2.4328 \cdot 10^{-3}$
0.025	$2.3853 \cdot 10^{-3}$	$1.8751 \cdot 10^{-3}$	$1.5517 \cdot 10^{-3}$	$1.3476 \cdot 10^{-3}$	$1.1716 \cdot 10^{-3}$

TABLE 2. $\max_{j,n}(\|\mathbf{X}_{num}(s_j, t^{(n)}) - (0, X_{2,r}^{mean}(t^{(n)}), c_l t^{(n)}) - \mathbf{X}_{alg}(s_j, t^{(n)})\|)$, for $r = M/8$, i.e., $j = N/4+1, \ldots, 3N/4+1$, $n = 0, 1, \ldots, 1260$, $M = 48$.

(44), of the order of $\mathcal{O}(10^{-5})$, $\mathcal{O}(10^{-2})$, which, in our opinion, given the nature of the problem, is reasonably good.

3.2.2. *Trajectory* $\mathbf{X}(0,t)$. The choice of the initial data (i.e., an even number of sides for $\mathbf{X}$) allows us to capture the time evolution of $\mathbf{X}(0,t)$. Due to the mirror symmetries of $\mathbf{X}$ explained in the Section 2.1.1, during the time evolution, the z-axis and $\mathbf{X}(-L/2 + kl/2, t)$, for $k = 0, 1, \ldots, 2M$, always lie in the same plane, for all $t \geq 0$, where an even value of k corresponds to the vertices, and an odd value, to the middle point of the sides. For instance, the numerical simulations show that $\mathbf{X}(0,t)$ lies in the YZ-plane, whereas $\mathbf{X}(-L/2 + lk, t)$, for $k = 0, 1, 2, \ldots, M$, lies in a plane that is the YZ-plane rotated by the time-like angle $L/2 - lk$ about the space-like z-axis in the counterclockwise direction. Thus, without loss of generality, we choose to observe the trajectory of $\mathbf{X}(0,t)$, and after projecting it onto $\mathbb{C}$, we define

$$z(t) = -X_2(0,t) + iX_3(0,t). \tag{45}$$

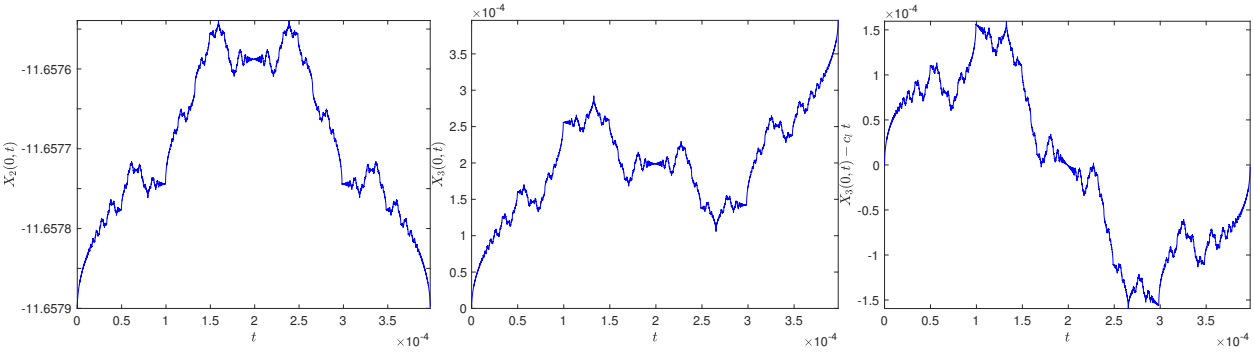

FIGURE 6. Left: $X_2(0,t)$. Center: $X_3(0,t)$. Right: $X_3(0,t) - c_l t$, i.e., the third component after removing the vertical height. In all the cases, $M = 192$, $l = 0.05$, $N/M = 2^{11}$.

On the other hand, after looking at $\mathbf{X}(0,t)$ componentwise, we note that its first and second components are periodic in time, while the third component becomes periodic after removing the constant vertical movement (see Figure 6, corresponding to the parameters $M = 192$, $l = 0.05$,

$N/M = 2^{11}$). Consequently, for a given value of l, we define

$$z_l(t) = z(t) - ic_l\ t,\ t \in [0, T_f], \tag{46}$$

which is T_f-periodic. Figure 7 shows both $z(t)$ and $z_l(t)$ side by side. The multifractal structure of $z_l(t)$ can be compared with the graph of

$$\phi(t) = \sum_{k=1}^{\infty} \frac{e^{i\pi k^2 t}}{i\pi k^2},\ t \in [0, 2]. \tag{47}$$

Let us mention that $\phi(t)$ appeared in [24], where its real part

$$f(t) = \sum_{k=1}^{\infty} \frac{\sin(\pi k^2 t)}{\pi k^2},$$

also called Riemann's non-differentiable function, was considered.

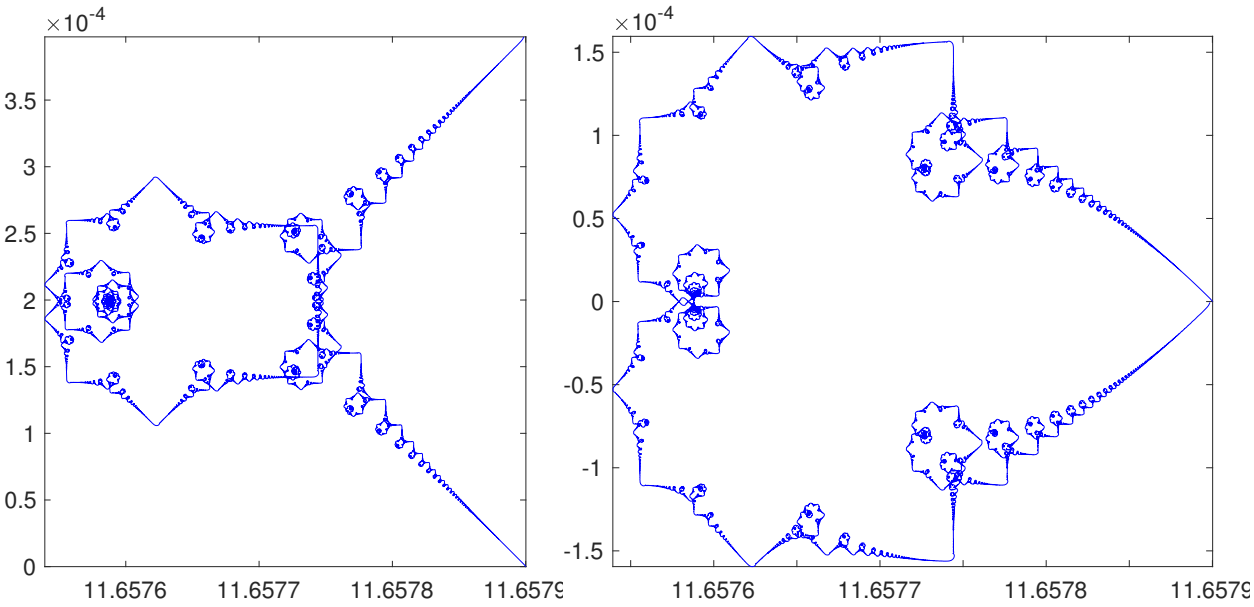

FIGURE 7. Left: $z(t)$. Right: $z_l(t)$. We took $M = 192$, $l = 0.05$, $N/M = 2^{11}$.

Remember that in the numerical simulations, for large values of M, the value of l needs to be chosen small; hence, we can have $z_l(t)$ only for certain values of l. However, the computation of the algebraic solutions depends neither on M nor it has any numerical error. As a result, we can work with any value of l (bearing in mind that, due to the exponential growth of $\mathbf{T}$, l can not be very large), and compute $z(t)$ algebraically. Since $\mathbf{X}_{alg}$ is determined up to a movement in the YZ-plane, if we take into account the trajectory along the y-axis to the planar curve, then $\mathbf{X}_{alg}(0, t)$ can be compared with $\phi(t)$. Furthermore, since the exact value of c_l is known, by giving the correct vertical

height, we can also obtain $z(t)$ algebraically. In other words, we define

$$\begin{cases} z_{l,alg}(t) = -(X_{2,alg}(0,t) + X_{2,alg}^{mean}(t)) + iX_{3,alg}(0,t), \\ z_{alg}(t) = z_{l,alg}(t) + ic_l t, \ t \in [0, T_f], \end{cases} \tag{48}$$

where $X_{2,alg}^{mean}(t)$ is the second component of (41). We also redefine the previous definition of $\phi(t)$ and write

$$\phi(t) = \sum_{k=1}^{\infty} \frac{e^{2\pi i k^2 t}}{k^2}, \ t \in [0,1]. \tag{49}$$

From now on, the purpose of working with $\mathbf{X}(0,t)$ will be twofold. First, we would like to see its dependence on the parameter l, and, second, we would want to compare its structure with the one in the Euclidean case. In order to address the latter question, we choose the value of l such that the corresponding parameter c_0 is kept the same in both the cases. More precisely,

$$\left[\frac{2}{\pi}\ln\left(\cosh\left(\frac{l}{2}\right)\right)\right]^{1/2} = \left[-\frac{2}{\pi}\ln\left(\cos\left(\frac{\pi}{M}\right)\right)\right]^{1/2} \Longleftrightarrow l = 2\,\mathrm{arccosh}\left(\sec\left(\frac{\pi}{M}\right)\right), \tag{50}$$

where M is the number of sides of the Euclidean regular planar M-polygon. Figure 8 shows $z_{l,alg}(t)$ (blue) for different values of l such that $M = 3, 4, 5, 6$ and 10 and $\phi(t)$ (red) where the respective intervals for t have been divided into 7561 points. Observe that, although similar, the shape of $z_{l,alg}$, for $M = 3$, is different from its Euclidean counterpart (see [18, Figure 3]); in Section 4.2, we will comment more on it. On the other hand, except for a scaling, the $z_{l,alg}(t)$ corresponding to the value $M = 10$ looks very close to $\phi(t)$. In order to further compare them, we employ two different approaches. First, for various values of l, we compute $\phi - \lambda_l z_{l,alg} - \mu_l$, where $\lambda_l \in \mathbb{R}$ and $\mu \in \mathbb{C}$ are given by the least squares fitting method (see [18, (73)]).

Thus, for l in (50), such that $M = 3, 4, \ldots, 20$, Figure 9 shows the absolute error $\max_t |(\phi(t) - \lambda_l z_{l,alg}(t) - \mu_l)|$ and the relative error $\max_t |(\phi(t) - \lambda_l z_{l,alg}(t) - \mu_l)/\phi(t)|$, where the maximum is taken over 7560 values. Clearly, as l gets smaller, the two errors decrease, hence showing that $z_{l,alg}$ converges to ϕ.

Using the fact that $z_{l,alg}(t)$ is T_f-periodic, we express the scaled $z_{l,alg}$ in terms of its Fourier expansion

$$z_{l,alg}^{scaled}(t) = \sum_{n=-\infty}^{\infty} d_{n,l}\, e^{2\pi i n t/T_f}, \ t \in [0, T_f],$$

where $z_{l,alg}^{scaled}(t) = \lambda_l z_{l,alg}(t) + \mu_l$, and compute its *fingerprint*, i.e., the plot of nd_n as a function of n. This approach was also employed in [25], where the Fourier coefficients d_n are approximated numerically through the `fft` algorithm in MATLAB. Figure 10 shows the fingerprint of $z_{l,alg}^{scaled}$, where l is given by (50), taking $M = 3, 5$ and 10. We observe that, as l becomes smaller, the dominating points (represented by blue stars) of $nd_{n,l}$ corresponding to the squares of n get closer to 1, while the rest of them get closer to 0. This allow us to conjecture that

$$\lim_{l\to 0} |n\, d_{n,l}| = \begin{cases} 1, & \text{if } n = k^2, k \in \mathbb{Z}, \\ 0, & \text{otherwise}, \end{cases}$$

which also shows the convergence in l of $z_{l,alg}^{scaled}$ to ϕ.

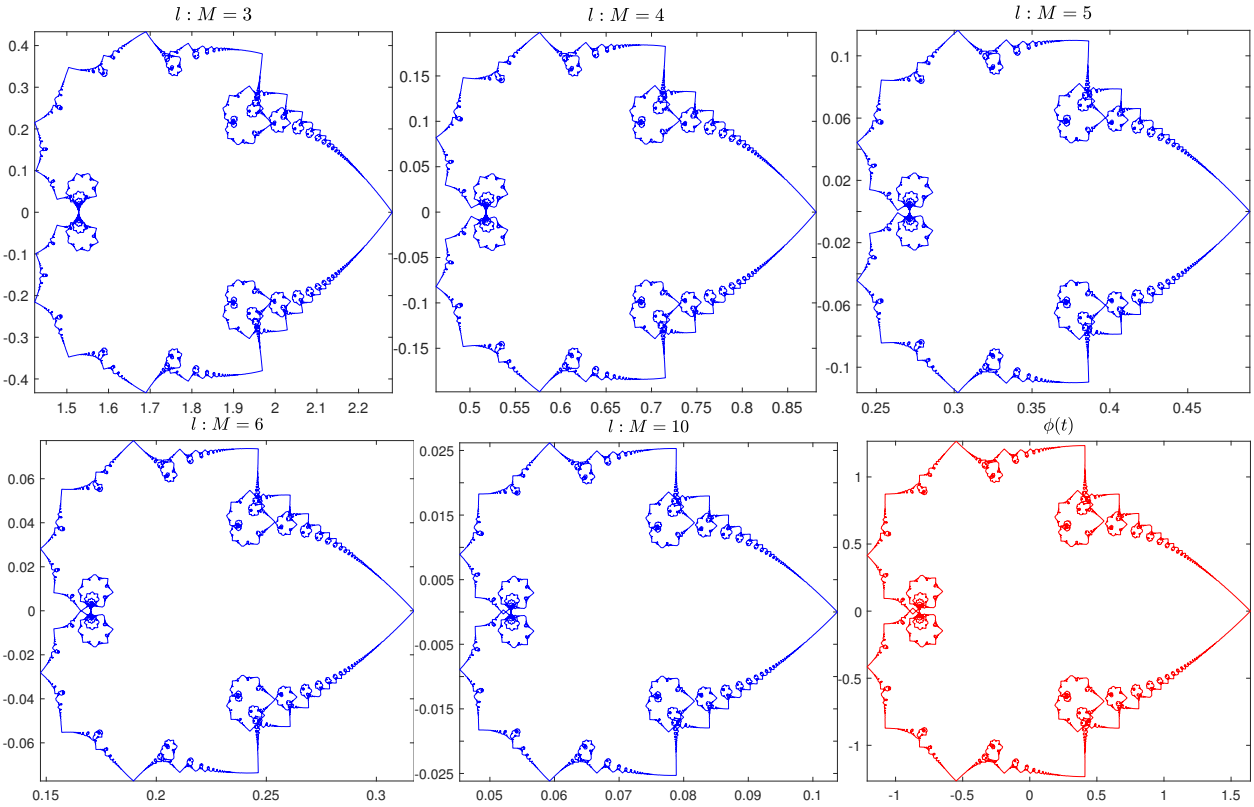

FIGURE 8. $z_l(t)$ (blue) and $\phi(t)$ (red). $z_l(t)$ has been generated for different values of l, computed using (50), for $M = 3, 4, 5, 6$ and 10. The parameter t takes its values in the respective intervals, which are divided into 7561 points.

3.3. $\mathbf{T}(s, t_{pq})$, $q \gg 1$. Having seen the evolution of regular M-polygons in the Euclidean case at rational times t_{pq}, with $q \gg 1$, we are curious about the behavior of a planar l-polygon [18, 25]. In this respect, as in [18], we have examined two cases; first, we consider t_{pq} with a *small* q and compute the evolution at $t = t_{pq} + \epsilon$, $|\epsilon| \ll 1$. We take $\epsilon = \frac{T_f}{q'}$, such that $q' \gg 1$, $\gcd(q, q') = 1$, and $\frac{p}{q} + \frac{1}{q'} = \frac{pq'+1}{qq'}$. Therefore, at $t_{pq} + \epsilon$, there will be qq' or $qq'/2$ times more sides. We consider the stereographic projection of $\mathbf{T}_{alg}$, projecting from $(-1, 0, 0)$; Figure 11 shows it for $M = 8$, $l = 0.6$, $p = 1$, $q = 3$, $q' = 7999$. One can note that 8×23997 values of the tangent vector form spiral-like structures whose center corresponds to the values of $\mathbf{T}$ at $t = T_f/3$. These spirals can be compared with the Cornu spiral which also appeared in [9, 18]. Next, we look at the rational times t_{pq}, with a *large* q, such that there is no pair $\tilde{p}, \tilde{q}$, with both $\tilde{q}$ and $|\frac{p}{q} - \frac{\tilde{p}}{\tilde{q}}|$ small. In particular, for the same parameters as before, we have taken $t = \left(\frac{1}{3} + \frac{1}{31} + \frac{1}{301}\right) T_f = \frac{10327}{27993} T_f$. The stereographic projection of $\mathbf{T}_{alg}$ is shown in Figure 11, where one can observe the spiral structures at a smaller scale, thus exhibiting a fractal-like phenomenon.

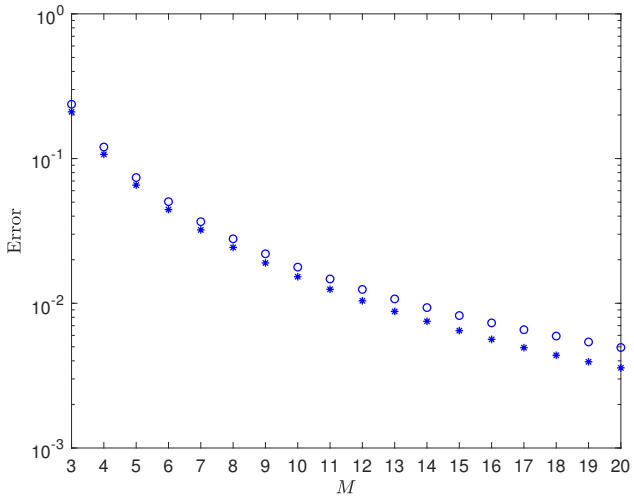

FIGURE 9. The maximum relative error (starred) and the absolute error (circled) between $\phi(t) = \sum_{k=1}^{\infty} e^{2i\pi k^2 t}/k^2$ and $z_{l,alg}(t)$. The sum for $\phi(t)$ has been computed for $k = 1, 2, \ldots, 2048$. Both $\phi(t)$ and $z_{l,alg}(t)$ have been evaluated at 7561 points.

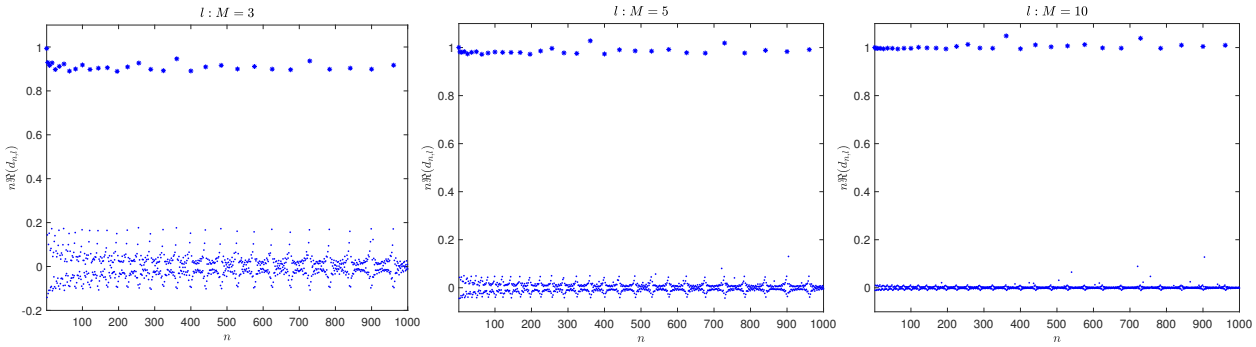

FIGURE 10. Fingerprint of $z_{l,alg}^{scaled}(t)$, where l is given by (50), taking $M = 3, 5, 10$.

4. Relationship between the l-polygon and one-corner problems

Following the approach in the Euclidean case, we conjecture that, at infinitesimal times, the l-polygon problem can be seen as a superposition of several one-corner problems [29]. In order to compare them, we solve the one-corner problem for $t = t_{1,q}$, $q \gg 1$, and rotate it in such a way that it is oriented with respect to the l-polygon problem. We denote the resulting solution by $\mathbf{X}_{rot}$, $\mathbf{T}_{rot}$, where $\mathbf{X}_{rot} = \mathbf{K} \cdot \mathbf{X}_{c_0}$, $\mathbf{T}_{rot} = \mathbf{K} \cdot \mathbf{T}_{c_0}$, with $\mathbf{X}_{c_0}$, $\mathbf{T}_{c_0}$ being the solution of the one-corner problem, for a certain matrix $\mathbf{K}$. Recall that

$$\lim_{s \to -\infty} \mathbf{T}_{c_0} = \mathbf{A}^- = (A_1, -A_2, -A_3)^T, \quad \lim_{s \to \infty} \mathbf{T}_{c_0} = \mathbf{A}^+ = (A_1, A_2, A_3)^T,$$

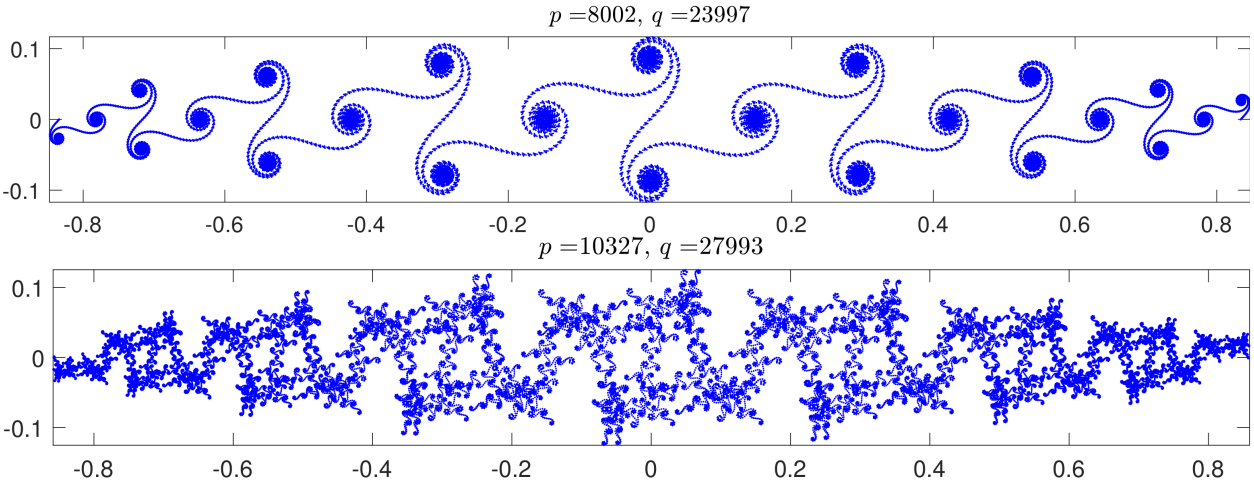

FIGURE 11. Stereographic projection of $\mathbf{T}_{alg}(s, t_{pq})$, for $M = 8$, $l = 0.6$.

and, thus, the matrix $\mathbf{K}$ can be computed by enforcing that $\lim_{s\to\pm\infty} \mathbf{T}_{rot}(s)$ corresponds to the tangent vector of l-polygon at $s = 0^{\pm}$, $t = 0$, i.e.,

$$\lim_{s\to-\infty} \mathbf{T}_{rot}(s) = (\cosh(l/2), -\sinh(l/2), 0)^T, \quad \lim_{s\to\infty} \mathbf{T}_{rot}(s) = (\cosh(l/2), \sinh(l/2), 0)^T.$$

More precisely,

$$\mathbf{K} = \begin{pmatrix} 1 & 0 & 0 \\ 0 & \dfrac{A_2}{\sqrt{A_2^2+A_3^2}} & \dfrac{A_3}{\sqrt{A_2^2+A_3^2}} \\ 0 & \dfrac{-A_3}{\sqrt{A_2^2+A_3^2}} & \dfrac{A_2}{\sqrt{A_2^2+A_3^2}} \end{pmatrix}, \tag{51}$$

which can be explicitly computed by using (64), (78), (79). Furthermore,

$$\begin{aligned} \mathbf{X}_{rot} &\equiv (X_{rot,1}, X_{rot,2}, X_{rot,3})^T = \mathbf{K}\cdot(X_{c_0,1}, X_{c_0,2}, X_{c_0,3})^T + \frac{l/2}{\sinh(l/2)}\mathbf{X}(0,0), \\ \mathbf{T}_{rot} &\equiv (T_{rot,1}, T_{rot,2}, T_{rot,3})^T = \mathbf{K}\cdot(T_{c_0,1}, T_{c_0,2}, T_{c_0,3})^T, \end{aligned} \tag{52}$$

where $\mathbf{X}(0,0)$ corresponds to the location of the corner of the planar l-polygon in (28).

4.1. **Numerical experiments.** To solve the two problems numerically, depending on whether q is even or odd, we consider the following discretization. For the l-polygon problem, given a value of q, we compute the algebraic solution $\mathbf{T}_{alg}(s, t_{1,q})$ at those values $s = s_k \in [-l/2, l/2]$ which belong to the middle points of the sides of the corresponding skew hyperbolic polygon. Thus, when q is odd, we choose $s_k = l(2k-1)/2q$, $k = -(q-1)/2, \ldots, (q+1)/2$, $\Delta s = s_{k+1} - s_k = l/q$; when $q/2$ is even, $s_k = l(2k-1)/q$, $k = -q/4+1, \ldots, q/4$, $\Delta s = 2l/q$; and when $q/2$ odd, $s_k = 2lk/q$, $k = -(q-2)/4, \ldots, (q-2)/4$, $\Delta s = 2l/q$. On the other hand, after discretizing the interval $[-l/2, l/2]$ into $2^4q + 1$ points with a step size $\Delta s = l/2^4q$, we solve the one-corner problem numerically. In this way, $\mathbf{T}_{c_0}(s, t_{1,q})$ can be computed for the same values $s = s_k$ as in the l-polygon problem, and then, from (51), we obtain $\mathbf{T}_{rot}(s, t_{1,q})$.

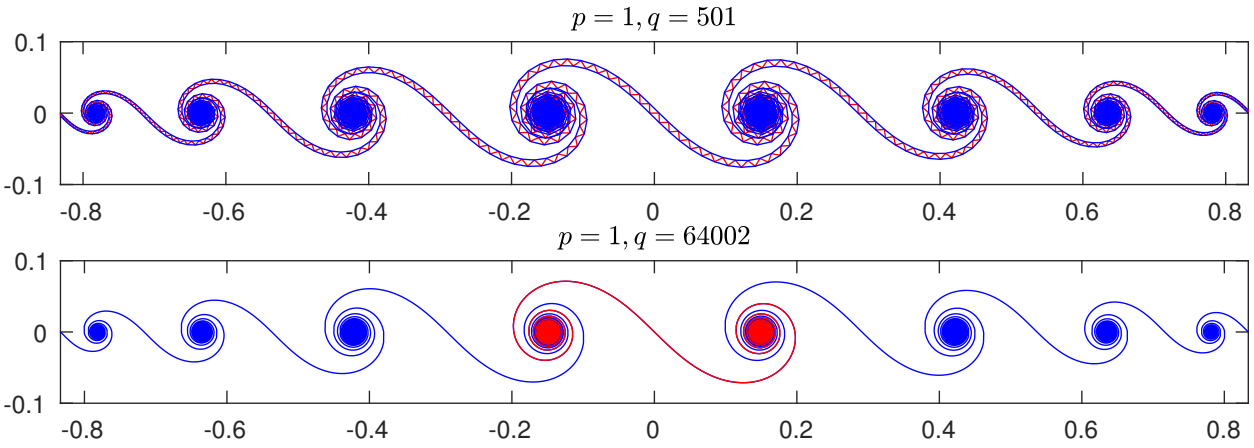

FIGURE 12. Stereographic projection of $\mathbf{T}_{alg}(s, t_{pq})$, for $M = 8$, $l = 0.6$.

q	Error	q	Error	q	Error
502	$4.4527 \cdot 10^{-5}$	4002	$5.5847 \cdot 10^{-6}$	32002	$6.9837 \cdot 10^{-7}$
1002	$2.2306 \cdot 10^{-5}$	8002	$2.7930 \cdot 10^{-6}$	64002	$3.4920 \cdot 10^{-7}$
2002	$1.1164 \cdot 10^{-5}$	16002	$1.3967 \cdot 10^{-6}$	128002	$1.7461 \cdot 10^{-7}$

TABLE 3. $|c_0 - \sqrt{t_{1,q}}\,|\mathbf{T}_{alg}(\Delta s, t_{1,q}) - \mathbf{T}_{alg}(-\Delta s, t_{1,q})|_0 / (2\Delta s)|$ where $c_0 = 0.1680\ldots$.

The first, second and third plots in Figure 13 show the error $\log_{10}(\|\mathbf{T}_{alg}(s_k, t_{1,q}) - \mathbf{T}_{rot}(s_k, t_{1,q})\|)$ against s_k, for $M = 8, l = 0.6$ and different values of q, where the Euclidean distance $\|\cdot\|$ is computed for each s_k. Note that, for a given q, the minimum error is attained at $s = 0$; moreover, we have plotted in red the minimum error in each case, which occurs at the biggest value of q. One can compare and observe that these plots follow a different, yet similar pattern as in the Euclidean case (see [29, Fig. 1]). Moreover, the maximum of the errors taken over all the values of s_k decreases as $\mathcal{O}(1/\sqrt{q}) = \mathcal{O}(t_{1,q})$. As in [29], the different shape of the error curve when q is odd, can be justified by plotting the corresponding $\mathbf{T}_{alg}(\cdot, t_{1,q})$. For instance, Figure 12 shows the stereographic projection of $\mathbf{T}_{alg}$ for $q = 501$, where the $Mq = 8 \times 501$ points (in red), when joined together, appear to form a curve with a sawtooth effect. However, if we plot only the alternate points (in blue), we obtain two smooth curves with the sawtooth structure in between, which in turn gets smaller approximately by a factor of one half when q is taken approximately four times bigger. This can be further appreciated in the fourth plot of Figure 13, where we measure the discrepancy between the two curves using $|\cdot|_0$ instead of $\|\cdot\|$.

On the other hand, for q even, we obtain a very regular smooth curve; see for instance Figure 12, where for $p = 1, q = 64002$, $\mathbf{T}_{alg}$(blue) and $\mathbf{T}_{rot}$(red) have been plotted together, and the red curve is visually indistinguishable from the blue one. Moreover, for q even, it is easy to approximate the coefficient c_0, and for that value, bearing in mind the one-corner problem, we write the curvature at $s = 0$ and $t > 0$ as $c_0(t) = \sqrt{t}|\mathbf{T}_s(0, t)|_0$ [9, 15]. Then, as in [29], at $t = t_{1,q}$, we approximate the derivative with respect to s using a finite difference. Without loss of generality, taking $q \equiv 2 \bmod 4$,

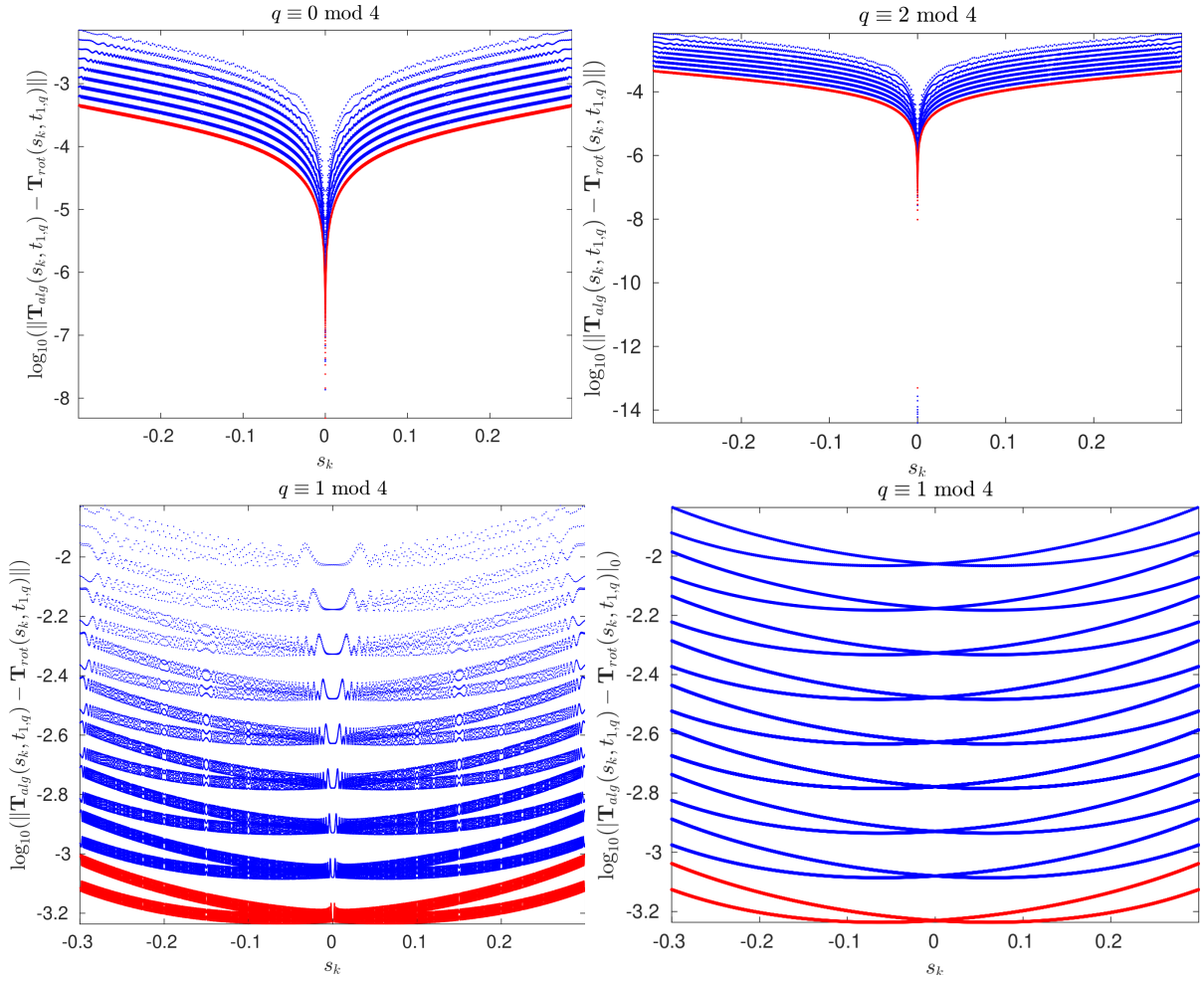

FIGURE 13. The error $\log_{10}(\|\mathbf{T}_{alg}(s_k,t_{1,q}) - \mathbf{T}_{rot}(s_k,t_{1,q})\|)$ for different values of q, for $l = 0.6$, $q \equiv 0 \bmod 4$, $q \equiv 2 \bmod 4$, $q \equiv 1 \bmod 4$; and the error $\log_{10}(|\mathbf{T}_{alg}(s_k,t_{1,q}) - \mathbf{T}_{rot}(s_k,t_{1,q})|_0)$, for $q \equiv 1 \bmod 4$.

we write

$$c_0 = \lim_{\substack{q\to\infty \\ q\equiv 2 \bmod 4}} \sqrt{t_{1,q}}\frac{|\mathbf{T}_{alg}(2l/q,t_{1,q}) - \mathbf{T}_{alg}(-2l/q,t_{1,q})|_0}{4l/q}, \tag{53}$$

where $\mathbf{T}_{alg}(s,t_{1,q})$ is continuous at $s = 0, 2l/q, -2l/q$. Next, using (35), we obtain

$$\begin{cases} \mathbf{T}_{alg}(2l/q,t_{1,q}) = (\cosh(l_q), \cos(\theta_1)\sinh(l_q), \sin(\theta_1)\sinh(l_q))^T, \\ \mathbf{T}_{alg}(-2l/q,t_{1,q}) = (\cosh(l_q), -\cos(\theta_{q-1})\sinh(l_q), -\sin(\theta_{q-1})\sinh(l_q))^T, \end{cases}$$

and, by substituting them in (53) and computing the limit, we get c_0 as in (25) (see [29, Section 2] for the intermediate steps). In Table 4.1, we display the error between c_0 and its approximated

value, computed using (53), for $l = 0.6$ and different values of q. Clearly, the error reduces as $\mathcal{O}(1/q)$, thus, showing a complete agreement between the two approaches.

Furthermore, we compare the time evolution of a point in the two problems and, thus, we compute $\mathbf{X}(0,t)$ and $\mathbf{X}_{rot}(0,t)$, for $t \in [0, t_{1,20}]$. More precisely, using (15),

$$\begin{aligned}\mathbf{X}_{rot}(0,t) &\equiv \mathbf{K}\cdot(X_{c_0,1}(0,0), X_{c_0,2}(0,0), X_{c_0,3}(0,0))^T + \frac{l/2}{\sinh(l/2)}\mathbf{X}(0,0)\\ &= 2c_0\sqrt{\frac{t}{A_2^2+A_3^2}}(0,A_3,A_2)^T + \frac{l/2}{\sinh(l/2)}\mathbf{X}(0,0).\end{aligned} \tag{54}$$

Both $\mathbf{X}(0,t)$ and $\mathbf{X}_{rot}(0,t)$ lie in the YZ-plane, and when plotting their projection onto $\mathbb{C}$ together, we note that, for small times, $\mathbf{X}(0,t)$ (in blue) can be very well approximated by a straight line (in red) with a slope A_2/A_3 (see the left-hand side of Figure 14). Furthermore, the plot of the third components $X_3(0,t)$, $X_{rot,3}(0,t)$ shows that the former grows along the curve $2c_0A_2\sqrt{t/(A_2^2+A_3^2)}$ (see the right-hand side of Figure 14).

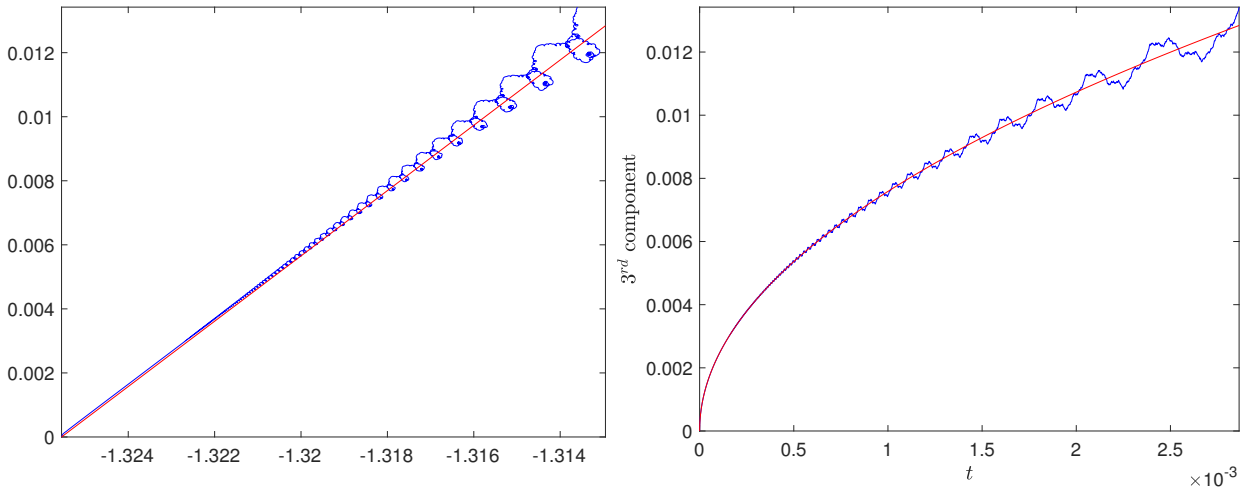

FIGURE 14. Left: $\mathbf{X}(0,t)$, $t \in [0, t_{1,20}]$, for $M = 8$, $l = 0.6$. Right: the third component versus time t, for the l-polygon problem (in blue) and for the one-corner problem (in red).

For our numerical simulations, we have taken $M = 8$, $l = 0.6$, but the results hold true for any $M \geq 2$, where M was chosen to be even in order to take advantage of the symmetries of the hyperbolic polygon. Thus, there is strong numerical evidence that, at small times, the l-polygon problem can be seen a superposition of several one-corner problems.

4.2. **Further remarks.** Note that the quantity A_2/A_3 also determines the angle φ that the curve $\mathbf{X}_{rot}(0,t)$ makes with the plane containing $\mathbf{X}_{rot}(s,0)$. Interestingly, φ is the angle corresponding to the corner of $z_l(t)$ located at $t = 0$, and this holds true for the Euclidean case as well. To compare the two cases simultaneously, from (50) we obtain c_0 for $M = 3, 4, \ldots, 20$, and compute A_2/A_3 using (78)-(79) in the hyperbolic case, and using [8, (57)] in the Euclidean case. The values thus obtained have been plotted in Figure 15, where it can be appreciated that A_2/A_3 is greater

(respectively, smaller) than the one in the hyperbolic (respectively, Euclidean) case, and tends to one, as c_0 becomes smaller; in fact, from (78)-(79), $A_2(0)/A_3(0) = 1$. On the other hand, in the hyperbolic case, we have

$$\varphi = \arctan\left(\frac{A_2}{A_3}\right) = \arctan\left(\frac{\Re\{\Upsilon\}}{\Im\{\Upsilon\}}\right) = \arg(i\bar{\Upsilon}), \tag{55}$$

with $\Upsilon = e^{i\pi/4}\Gamma(1 - ic_0^2/4)\Gamma(1/2 + ic_0^2/4)$. Thus, for a given c_0, φ is larger (respectively, smaller) than $\pi/2$ and, in the limit, it converges to $\pi/2$, as in the case of Riemann's non-differentiable function.

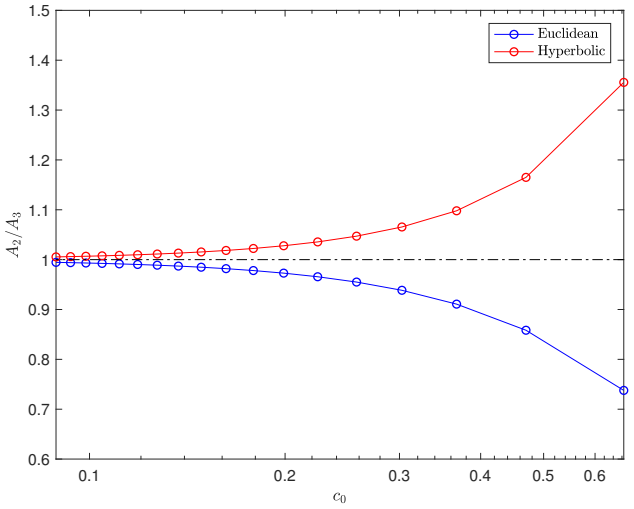

FIGURE 15. Semilogarithmic plot of A_2/A_3 as a function of c_0. Clearly, as c_0 tends to 0, A_2/A_3 tends to 1 (dashed dotted line).

The relationship between the l-polygon problem and the one-corner problem has several deep implications. One of these is the computation of the speed of the center of mass c_l, as defined in (39). Following the arguments in [29], c_l can be obtained by computing the integral of $\mathbf{X}_{rot,3}(s/\sqrt{t}, 1) = \mathbf{X}_{rot,3}(s,t)$. Thus, we have:

Theorem 2.

$$\int_{-\infty}^{\infty} \mathbf{X}_{rot,3}(s)\ ds = \frac{2\pi c_0^2}{\sqrt{1 - e^{-\pi c_0^2}}}. \tag{56}$$

Therefore, we can obtain c_l in terms of c_0 and in terms of l:

$$c_l = \frac{2\pi c_0^2}{l\sqrt{1 - e^{-\pi c_0^2}}} = \frac{4\ln\cosh(l/2)}{l\sqrt{1 - \operatorname{sech}^2(l/2)}} = -\frac{\ln(1 - \tanh^2(l/2))}{l/2\tanh(l/2)}. \tag{57}$$

We omit the proof as it follows similar steps to those in [29, Theorem 3.1]. Moreover, by applying (51) in (15)-(16) and integrating the resulting initial value problem numerically as in [29, Section 3.3], we also have a numerical justification of Theorem 2.

5. Expression for $\mathbf{A}^{\pm} = (A_1, \pm A_2, \pm A_3)^T$

For the one-corner problem in the Euclidean case, a precise expression for each of the components of the tangent vector $\mathbf{A}^+ = (A_1, A_2, A_3)^T$ was given in [8]; and, later in [9], an expression for A_1, i.e., (18) was obtained for the hyperbolic case as well. In the following lines, using a completely different approach, we rederive A_1 by means of the Laplace transform, and, continuing the calculations in [9], we calculate A_2 and A_3, whose knowledge has been extremely useful in Section 4.

5.1. **Computation of A_1 using the Laplace transform.** Recall that the proof of Theorem 2 mainly involves working with the even solution of (17), which is also analytic. However, in the following lines, we consider the odd solution, which behaves like δ' near the origin and can be expressed as

$$\hat{\chi}(\xi) = b_0\delta' + b_1 \operatorname{sgn}(\xi) + b_2 \operatorname{sgn}(\xi)\xi + \dots,$$

where the coefficients $b_0 = 1, b_1 = -c_0^2, b_2 = -c_0^4/(1-4c_0^2), \dots$, are obtained by introducing $\hat{\chi}(\xi)$ in (17). If we write the first component of $\hat{\mathbf{X}}(\xi)$ as $\hat{X}_1(\xi) = -iA_1\hat{\chi}(\xi)$, and define

$$\widehat{W}_1(\eta) = \widehat{W}_1(\xi^2) = \xi^2 \hat{X}_1(\xi),\ \eta > 0,$$

then it solves

$$\widehat{W}'' + \widehat{W}\left(1 + \frac{c_0^2}{\eta}\right) = 0 \Leftrightarrow \eta\widehat{W}'' + \eta\widehat{W} + c_0^2\widehat{W} = 0, \tag{58}$$

with

$$\widehat{W}_1(0) = 0,\ \widehat{W}_1'(0) = \lim_{\eta\to 0}\frac{\widehat{W}_1(\eta)}{\eta} = iA_1c_0^2. \tag{59}$$

On the other hand, the Laplace transform of $\widehat{W}_1(\eta)$:

$$\mathcal{L}(t) = \mathcal{L}\{\widehat{W}_1(\eta)\} = \int_0^\infty \widehat{W}_1(\eta)e^{-t\eta}d\eta,\ t > 0, \tag{60}$$

satisfies

$$t^2\mathcal{L}'(t) + 2t\mathcal{L}(t) + \mathcal{L}'(t) - c_0^2\mathcal{L}(t) = 0. \tag{61}$$

Furthermore,

$$\mathcal{L}(0) = \int_0^\infty \widehat{W}_1(\eta)d\eta = 2\int_0^\infty \xi^3\hat{X}_1(\xi)d\xi = \int_{-\infty}^\infty \xi^3\hat{X}_1(\xi)d\xi = iX_1'''(0) = ic_0^2, \tag{62}$$

where we have used the fact that $\hat{X}_1$ is odd. Rewriting (60) as

$$\mathcal{L}(t) = \int_0^\infty \widehat{W}_1(\eta)e^{-t\eta}d\eta = \frac{1}{t}\int_0^\infty \widehat{W}_1'(\eta)e^{-t\eta}d\eta = \frac{\widehat{W}_1'(0)}{t^2} + \frac{1}{t^2}\int_0^\infty \widehat{W}_1''(\eta)e^{-t\eta}d\eta,$$

we have

$$t^2\mathcal{L}(t) = \widehat{W}_1'(0) + \int_0^\infty \widehat{W}_1''e^{-t\eta}d\eta,$$

which, as $t \to \infty$, becomes

$$\lim_{t\to\infty} t^2\mathcal{L}(t) = \widehat{W}'(0). \tag{63}$$

Hence, from (61)-(62), we have an initial value problem whose solution $\mathcal{L}(t)$ gives

$$\lim_{t\to\infty} t^2\mathcal{L}(t) = \lim_{t\to\infty} t^2 \frac{\mathcal{L}(0)}{1+t^2} e^{c_0^2 \arctan(t)} = ic_0^2 e^{c_0^2\pi/2}.$$

Combining this with (59), (63), we conclude that

$$ic_0^2 A_1 = \widehat{W}'(0) = ic_0^2 e^{c_0^2\pi/2} \implies A_1 = e^{c_0^2\pi/2}. \tag{64}$$

The above approach works the same for the Euclidean case as well; hence, one can obtain at the corresponding expression for A_1.

5.2. **Computation of A_2 and A_3.** By continuing the computations of [9, Theorem 1], we can also obtain the expressions for A_2, A_3. In this regard, writing them componentwise, the solutions of the Frenet–Serret formulas with $\kappa = c_0$, $\tau = s/2$, i.e., $\mathbf{T} \equiv (T_j)$, $\mathbf{n} \equiv (n_j)$, $\mathbf{b} \equiv (b_j)$, satisfy

$$|n_j|^2 + |b_j|^2 - |T_j|^2 = \begin{cases} -1, & \text{if } j = 1, \\ 1, & \text{if } j = 2, 3, \end{cases}$$

where

$$\mathbf{T}(0) = (1,0,0)^T,\ \mathbf{n}(0) = (0,1,0)^T,\ \mathbf{b}(0) = (0,0,1)^T.$$

Recall that, from [9, Theorem 1], $A_j = \lim_{s\to\infty} T_j(s),\ j = 1,2,3$, with

$$T_j(s) = i(1 + \theta_j\bar{\vartheta}_j)(s),\ j = 2,3, \tag{65}$$

where θ_j and ϑ_j satisfy

$$\begin{cases} \theta_j'' + i(s/2)\theta_j' - (c_0^2/4)\theta_j = 0 \\ \vartheta_j'' + i(s/2)\vartheta_j' - (c_0^2/4)\vartheta_j = 0 \\ \theta_j'\bar{\vartheta}_j' - (c_0^2/4)\theta_j\bar{\vartheta}_j = E_j, \end{cases} \tag{66}$$

and can be represented as

$$\begin{cases} \theta_j(s) = a_{1,j}\beta_1(s) + a_{2,j}\beta_2(s), \\ \vartheta_j(s) = b_{1,j}\beta_1(s) + b_{2,j}\beta_2(s), \end{cases} \tag{67}$$

where E_j is chosen later, and $\beta_1(s)$, $\beta_2(s)$ are as in [9, (55)]. Hence, our first goal is to compute $a_{1,j}, a_{2,j}, b_{1,j}, b_{2,j}$, for $j = 2,3$.

Differentiating (67) gives

$$\begin{cases} \theta_j'(s) = a_{1,j}\beta_1'(s) + a_{2,j}\beta_2'(s), \\ \vartheta_j'(s) = b_{1,j}\beta_1'(s) + b_{2,j}\beta_2'(s), \end{cases} \tag{68}$$

and, from [9, p. 77], for $j = 2,3$, the asymptotics of $\theta_j(s)$ and $\vartheta_j(s)$ are given by

$$\begin{cases} \theta_j(s) = (a_{1,j}\gamma_1 + a_{2,j}\gamma_2)e^{-i\frac{c_0^2}{2}\log s} + \mathcal{O}(1/s),\ s\to\infty, \\ \vartheta_j(s) = (b_{1,j}\gamma_1 + b_{2,j}\gamma_2)e^{-i\frac{c_0^2}{2}\log s} + \mathcal{O}(1/s),\ s\to\infty, \end{cases} \tag{69}$$

where

$$\gamma_1 = 2e^{-\pi c_0^2/4}\Gamma(1 + ic_0^2/2),\ \gamma_2 = -2e^{\pi c_0^2/4}\Gamma(1 + ic_0^2/2).$$

By taking $E_2 = c_0^2/2$, $T_2(0) = 0$ in (65), we get

$$\theta_2'(0)\bar{\vartheta}_2(0) = c_0^2/4, \tag{70}$$

and from [9, (53)]

$$n_j - ib_j = (2i/c_0)\theta_j\bar{\vartheta}_j', \tag{71}$$

so, if $\theta_2(0) = 1$, then, by using (65), (70), we obtain

$$\theta_2'(0) = ic_0/2,\ \bar{\vartheta}_2(0) = -1, \bar{\vartheta}_2'(0) = -ic_0/2. \tag{72}$$

Thus, by evaluating (67), (68) at $s = 0$, and using $\beta_1(0) = -\beta_2(0)$, $\beta_1'(0) = \beta_2'(0)$, and (72),

$$\begin{cases} (a_{1,2} - a_{2,2})\beta_1 = 1,\ (a_{1,2} + a_{2,2})\beta_1' = ic_0/2, \\ (b_{1,2} - b_{2,2})\beta_1 = -1,\ (b_{1,2} + b_{2,2})\beta_1' = ic_0/2, \end{cases} \tag{73}$$

where

$$\beta_1 \equiv \beta_1(0) = 2e^{-\pi c_0^2/8}\Gamma(1 + ic_0^2/4), \quad \beta_1' \equiv \beta_1'(0) = -(c_0^2/2)e^{i\pi/4}e^{-\pi c_0^2/8}\Gamma(1/2 + ic_0^2/4).$$

As a result,

$$a_{1,2} = \frac{ic_0\beta_1 + 2\beta_1'}{4\beta\beta_1'},\ a_{2,2} = \frac{ic_0\beta_1 - 2\beta_1'}{4\beta\beta_1'},\ b_{1,2} = \frac{ic_0\beta_1 - 2\beta_1'}{4\beta\beta_1'},\ b_{2,2} = \frac{ic_0\beta_1 + 2\beta_1'}{4\beta\beta_1'}. \tag{74}$$

Similarly, for $j = 3$, taking $E_3 = c_0^2/2$, $\theta_3(0) = i$, and continuing in the same way yields

$$a_{1,3} = i\frac{-c_0\beta_1 + 2\beta_1'}{4\beta\beta_1'},\ a_{2,3} = -i\frac{c_0\beta_1 + 2\beta_1'}{4\beta\beta_1'},\ b_{1,3} = -i\frac{c_0\beta_1 + 2\beta_1'}{4\beta\beta_1'},\ b_{2,3} = i\frac{-c_0\beta_1 + 2\beta_1'}{4\beta\beta_1'}. \tag{75}$$

Remember that our aim is to compute A_j, which, from (65) and (69) implies computing

$$\lim_{s\to\infty} \theta_j(s)\bar{\vartheta}_j(s) = (a_{1,j}(s)\gamma_1 + a_{2,j}(s)\gamma_2)\left(\overline{b_{1,j}(s)\gamma_1 + b_{2,j}(s)\gamma_2}\right),\ j = 2, 3.$$

Therefore, from (74),

$$\lim_{s\to\infty} \theta_2(s)\bar{\vartheta}_2(s) = \left(\frac{ic_0}{4\beta_1'}(\gamma_1 + \gamma_2) + \frac{1}{2\beta_1}(\gamma_1 - \gamma_2)\right)\overline{\left(\frac{ic_0}{4\beta_1'}(\gamma_1 + \gamma_2) - \frac{1}{2\beta_1}(\gamma_1 - \gamma_2)\right)}, \tag{76}$$

and by using the following identities for $y \in \mathbb{R}$:

$$\begin{aligned} |\Gamma(1 + iy)|^2 = y^2|\Gamma(iy)|^2, \quad |\Gamma(iy)|^2 = \frac{\pi}{y\sinh\pi y}, \\ |\Gamma(1/2 + iy)|^2 = \frac{\pi}{\cosh\pi y}, \quad \overline{\Gamma(1 + iy)} = \Gamma(1 - iy), \end{aligned} \tag{77}$$

we obtain

$$|\gamma_1 - \gamma_2|^2 = 4\pi c_0^2\frac{(1 + e^{-\pi c_0^2/2})^2}{1 - e^{-\pi c_0^2}},\ |\gamma_1 + \gamma_2|^2 = \pi c_0^2\frac{e^{-\pi c_0^2/4}}{\sinh(\pi c_0^2/4)},\ (\gamma_1 - \gamma_2)\overline{(\gamma_1 + \gamma_2)} = -4c_0^2\pi.$$

Consequently, we can write

$$\begin{aligned} A_2 &= \lim_{s\to\infty} T_2(s) = \lim_{s\to\infty} T_2(s)(1 + \theta_2(s)\bar{\vartheta}_2(s)) \\ &= \frac{2}{\pi c_0}e^{\pi c_0^2/4}\sinh(\pi c_0^2/2)\Re\{e^{i\pi/4}\Gamma(1 - ic_0^2/4)\Gamma(1/2 + ic_0^2/4)\} \\ &= \frac{2}{\pi c_0}e^{\pi c_0^2/4}\sinh(\pi c_0^2/2)\Re\{\Upsilon\}, \end{aligned} \tag{78}$$

with $\Upsilon = e^{i\pi/4}\Gamma(1 - ic_0^2/4)\Gamma(1/2 + ic_0^2/4) = \frac{\sqrt{\pi}}{2}\, e^{i\pi/4}B(1 - ic_0^2/4, 1/2 + ic_0^2/4)$, where $B(\cdot,\cdot)$ is the beta function. Finally, using (75) and following same steps as above, one can arrive at

$$A_3 = \frac{2}{\pi c_0} e^{\pi c_0^2/4} \sinh(\pi c_0^2/2)\Im\{\Upsilon\}. \tag{79}$$

6. Conclusions

In this article, we have studied the evolution of (5)-(6) for a regular planar l-polygon. The motivation to work with such kind of initial data indeed comes from the one-corner problem in the hyperbolic case [9], and recent work on the regular polygons in the Euclidean case [18]. In [9], it was observed that, due to the exponential growth of the Euclidean length of the tangent vector, the numerical treatment of the one-corner problem in the hyperbolic case poses restrictions on the value of the parameter c_0, and the same is observed in the planar l-polygon case as well. After trying several different numerical schemes, we have concluded that a finite difference scheme with fixed boundary conditions on $\mathbf{T}$ gives the best results, which are also in agreement with their algebraic counterparts. The evolution is periodic in time with a period $l^2/2\pi$, and at intermediate rational times $t_{pq} = (l^2/2\pi)(p/q)$, $\gcd(p, q) = 1$, depending on the parity of q, the polygonal curve has q or $q/2$ times more sides. As in the Euclidean case, this intermittent behavior of formation/annihilation of the corners can be seen as a nonlinear Talbot effect [18, 29].

We have also analyzed the multifractal trajectory of a corner $\mathbf{X}(0, t)$ by comparing it with Riemann's non-differentiable function and its equivalent in the Euclidean case; this has been supported with adequate numerical experiments. Furthermore, as in [29], we have established a relationship between the one-corner problem and the l-polygon problem, and, as a consequence, an exact expression for the speed of the center of mass of an l-polygon has been obtained. Finally, we have obtained explicit expressions for the components of the tangent vector $\mathbf{A}^{\pm}$, whose knowledge has been essential in this work.

Acknowledgments

Sandeep Kumar would like to thank Carlos J. García-Cervera for the discussions on Section 3 which took place during his visit to the University of California, Santa Barbara, USA.

This paper was partially supported by the ERCEA Advanced Grant 2014 669689 - HADE, by the MICINN Projects PGC2018-094522-B-I00 and SEV-2017-0718, by the Basque Government Grant IT1247-19, and by the Basque Government BERC Program 2018-2021.

References

[1] L. S. D. Rios, "Sul moto d'un liquido indefinito con un filetto vorticoso di forma qualunque," *Rendiconti del Circolo Matematico di Palermo (1884-1940)*, vol. 22, no. 1, pp. 117–135, 1906. In Italian.
[2] R. J. Arms and F. R. Hama, "Localized-Induction Concept on a Curved Vortex and Motion of an Elliptic Vortex Ring," *Physics of Fluids*, vol. 8, no. 4, pp. 553–559, 1965.
[3] B. Khesin, "The vortex filament in any dimension," *Procedia IUTAM*, vol. 7, pp. 135–140, 2013.
[4] Q. Ding, "A note on the NLS and the Schrödinger flow of maps," *Physics Letters A*, vol. 248, pp. 49–56, 1998.
[5] J. G. Ratcliffe, *Foundations of Hyperbolic manifolds*. Graduate texts in Mathematics, volume 149, Springer, New York, second edition, 2006.
[6] R. López, "Differential Geometry of Curves and Surfaces in Lorentz-Minkowski space," *arXiv:0810.3351*, 2008.
[7] H. Hasimoto, "A soliton on a vortex filament," *Journal of Fluid Mechanics*, vol. 51, no. 3, pp. 477–485, 1972.

[8] S. Gutiérrez, J. Rivas, and L. Vega, "Formation of singularities and self-similar vortex motion under the localized induction approximation," *Communications in Partial Differential Equations*, vol. 28, no. 5–6, pp. 927–968, 2003.
[9] F. de la Hoz, "Self-similar solutions for the 1-D Schrödinger map on the hyperbolic plane," *Mathematische Zeitschrift*, vol. 257, no. 1, pp. 61–80, 2007.
[10] V. Banica and L. Vega, "On the Stability of a Singular Vortex Dynamics," *Communications in Mathematical Physics*, vol. 286, no. 2, pp. 593–627, 2009.
[11] V. Banica and L. Vega, "Scattering for 1D cubic NLS and singular vortex dynamics," *Journal of the European Mathematical Society (JEMS)*, vol. 14, no. 1, pp. 209–253, 2012.
[12] V. Banica and L. Vega, "Stability of the Self-similar Dynamics of a Vortex Filament," *Archive for Rational Mechanics and Analysis*, vol. 210, no. 3, pp. 673–712, 2013.
[13] V. Banica and L. Vega, "The initial value problem for the Binormal Flow with rough data," *Annales scientifiques de l'ENS*, vol. 48, no. 6, pp. 1421–1453, 2015.
[14] T. F. Buttke, "A Numerical Study of Superfluid Turbulence in the Self-Induction Approximation," *Journal of Computational Physics*, vol. 76, no. 2, pp. 301–326, 1998.
[15] F. de la Hoz, C. J. García-Cervera, and L. Vega, "A Numerical Study of the Self-Similar Solutions of the Schrödinger Map," *SIAM Journal on Applied Mathematics*, vol. 70, no. 4, pp. 1047–1077, 2009.
[16] R. L. Jerrard and D. Smets, "On Schrödinger maps from T^1 to S^2," *Annales scientifiques de l'École Normale Supérieure (4)*, vol. 45, no. 4, pp. 637–680, 2012.
[17] R. L. Jerrard and D. Smets, "On the motion of a curve by its binormal curvature," *Journal of the European Mathematical Society*, vol. 17, no. 6, pp. 1487–1515, 2015.
[18] F. de la Hoz and L. Vega, "Vortex filament equation for a regular polygon," *Nonlinearity*, vol. 27, no. 12, pp. 3031–3057, 2014.
[19] M. V. Berry and S. Klein, "Integer, fractional and fractal Talbot effects," *Journal of Modern Optics*, vol. 43, pp. 2139–2164, 1996.
[20] M. B. Erdoğan and N. Tzirakis, "Talbot effect for the cubic non-linear Schrödinger equation on the torus," *Mathematical Research Letters*, vol. 20, no. 6, pp. 1081–1090, 2013.
[21] P. J. Olver, "Dispersive quantization," *The American Mathematical Monthly*, vol. 117, no. 7, pp. 599–610, 2010.
[22] F. F. Grinstein and E. J. Gutmark, "Flow control with noncircular jets," *Annual Review of Fluid Mechanics*, vol. 31, pp. 239–272, 1999.
[23] F. F. Grinstein, E. J. Gutmark, and T. Parr, "Nearfield dynamics of subsonic, free square jets. A computational and experimental study," *Physics of Fluids*, vol. 7, pp. 1483–1497, 1995.
[24] J. J. Duistermaat, "Selfsimilarity of "Riemann's Nondifferentiable function"," *Nieuw Archief voor Wiskunde*, vol. (4) 9, no. 3, pp. 303–337, 1991.
[25] F. de la Hoz, S. Kumar, and L. Vega, "On the Evolution of the Vortex Filament Equation for regular M-polygons with nonzero torsion," *SIAM Journal on Applied Mathematics*, vol. 80, no. 2, pp. 1034–1056, 2020.
[26] V. Banica and L. Vega, "Evolution of polygonal lines by the binormal flow," *arXiv:1807.06948*, 2018. to appear in Annals of PDE.
[27] V. Banica and L. Vega, "On the energy of critical solutions of the binormal flow," *arXiv:1907.08789*, 2019. to appear in Communications in Partial Differential Equations.
[28] F. Fillastre., "Polygons of the Lorentzian plane and spherical simplexes," *Elemente der Mathematik, European Mathematical Society*, vol. 69, no. 3, pp. 144–155, 2014.
[29] F. de la Hoz and L. Vega, "On the Relationship between the One-Corner Problem and the M-Corner Problem for the Vortex Filament Equation," *Journal of Nonlinear Science*, vol. 28, no. 6, pp. 2275–2337, 2018.
[30] R. L. Bishop, "There is More than One Way to Frame a Curve," *The American Mathematical Monthly*, vol. 82, no. 3, pp. 246–251, 1975.
[31] M. Özdemir and M. Erdoğdu, "On the Rotation Matrix in Miknowski Space-Time," *Reports on Mathematical Physics*, vol. 74, no. 1, pp. 27–38, 2014.

(F. de la Hoz) Department of Applied Mathematics and Statistics and Operations Research, Faculty of Science and Technology, University of the Basque Country UPV/EHU, Barrio Sarriena S/N, 48940 Leioa, Spain

E-mail address: francisco.delahoz@ehu.eus

(S. Kumar) BCAM - Basque Center for Applied Mathematics, Alameda de Mazarredo 14, 48009 Bilbao, Spain.

E-mail address: skumar@bcamath.org

(L. Vega) BCAM, Department of Mathematics, Faculty of Science and Technology, University of the Basque Country UPV/EHU, Barrio Sarriena S/N, 48940 Leioa, Spain

E-mail address: luis.vega@ehu.eus, lvega@bcamath.org